A kinking-based failure model for engineering simulation of compressive crushing of composite structures

(article starts on next page)

A kinking-based failure model for engineering simulation of compressive crushing of composite structures

Niklas Jansson [a], Martin Fagerström [b,*]

[a] *FS Dynamics Sweden AB, Mölndalsvägen 24, SE-412 63 Gothenburg, Sweden*
[b] *Chalmers University of Technology, Department of Industrial and Materials Science, SE-412 96 Gothenburg, Sweden*

A B S T R A C T

The use of continuum damage models is state of the art for the finite element modelling of progressive damage and failure under compressive loading in composites during e.g. crash and impact simulations. However, after failure initiation the compressive stress is quickly degraded to zero alternatively to a plateau with constant stress and at a certain point the element needs to be deleted due to the damage level or large element deformation. This effectively represent a void in the material which contrasts with reality where a fully formed kink band would be expected to have compressive properties similar to the transverse direction of the ply. To better represent this physical behaviour is here a kinking formulation developed that instead of the common constant stress plateau after initial softening features a stiffening at larger strains. This formulation has been implemented in a commercial FE-code complemented by criteria for kinking initiation and kink band broadening. The results presented show the novelty of the model in that it describes a chain of events starting with initiation of kinking, progressing to the growth of kink bands through the element and finally including an increase in stress that initiate kinking in adjacent elements.

1. Introduction

Advanced composite materials with continuous fibres are commonly employed in structures within e.g. the energy and marine sectors but also in more high performance applications within sports equipment, aeronautical and automotive industry. For most applications, the structures are designed to not fail under static and fatigue loads using finite element analysis with suitable failure criteria and safety factors. For cars and aircrafts there are also requirements on the crashworthiness of the structure, i.e. requirements on the integrity and energy absorption characteristics of the structure under crash loadings. For composites this involves several damage and fracture mechanisms as fibre tensile and compressive fracture, matrix cracking and delaminations rather than the plastic deformations seen in metallic structures. In order to model this within a finite element setting, continuum damage mechanics models are applied where the regular fracture initiation criteria are complemented by a damage evolution law to model the progressive damage response and represent the gradual softening of the material all the way up to complete loss of load bearing capacity [1–3]. The damage law is commonly a linear reduction of the stress with increasing strain after fracture initiation and the reduction rate is determined so that the energy dissipated during the damage process is equal to the fracture toughness [1,2]. This is used also for compressive failure although this way of modelling represents the formation of a crack in the structure and hence effectively introduces a void in the structure. To account for the case where crushing of a composite structure is analysed, e.g. in crashworthiness simulations of energy absorbing structures, the traditional linear stress reduction for compressive failure has been complemented with a plateau at constant stress, with the aim to obtain a correct resulting crushing stress [2,3]. The crush stress plateau value needs to be calibrated against crushing data. However, it does not only depend on the intralaminar ply behaviour but also on the laminate lay-up and, in many cases, also the structural geometry. Therefore, it can not necessarily be determined for one lay-up and then used for another. Constitutive models that include a stress plateau in compression is also implemented in commercial FE-codes, i.e. mat054 and mat058 in Ls-Dyna [4].

The compressive failure of composites is attributed to fibre kinking and growth of kink bands [5,6]. Compared to crack propagation in tension, the broadening of the damage height during growth of kink bands makes it difficult to measure the intralaminar fracture toughness in compression [7]. An alternative to measure the intralaminar fracture

---

* Corresponding author.
  E-mail address: martin.fagerstrom@chalmers.se (M. Fagerström).

toughness is the use of micro-mechanical based kinking models that predict the softening behaviour from the 3-D stress state and the shear stress–strain behaviour of the composite [8,9]. The foundation of this theory is based on analysis of the shear stresses that are required for equilibrium of miss-aligned fibres under compressive load. Argon [10] introduced this kind of model and derived an expression for the compressive strength as function of fibre miss-alignment and shear strength. Budiansky [11] used an elastic-perfectly plastic model which also included the kink band angle β. This model was later extended to include hardening plasticity and the effect of global shear loads [12]. More general non-linear stress–strain relations for the shear behaviour has also been used to predict compressive failure due to kinking [13,14].

Kink bands are described in terms of an angle to the load direction β and a band width. Studies into kinking failure show the formation of multiple kink bands [15–17] and controlled deformation experiments have shown that kink bands can increase in width (kink band broadening), either without fibre breaks in the case of ductile fibres [18,19] or by formation of new kink bands adjacent to the existing ones [20,21]. Models that can predict the compressive stress necessary to sustain this kink band broadening mechanism has been developed and compared to experimental results [18,22].

Fundamentally the use of continuum damage mechanics models, where the stiffness is degraded to a low value or even zero, implies that large compressive deformations can take place with low or no resistance. As the large compressive strains are not compensated with deformations in other directions, this also means that the volume of the material is decreasing. In a finite element setting this is amplified due to the deletion of elements with large deformations or low stiffness due to damage. An addition of a stress plateau to the compression response as described in Ref. [3] delays but does not prohibit the element deletion. Physically the kinking failure will lead to an initial softening when the kink band is formed but a considerable stiffness remains and will prohibit large compressive deformations. This work presents a compressive failure formulation based on a kinking model developed with this specific behaviour in mind. The objective with the compressive failure formulation is therefore not to predict the kinking failure in detail, instead it is developed in order to model the compressive response beyond the failure initiation, i.e. for simulation of confined compaction or crushing. The developed kinking model displays a stiffening behaviour at large compressive strains which prohibits excessive deformations that otherwise would result in element deletion to avoid a significant reduction of critical time step size in the explicit FE simulations. The kinking formulation is similar to the theory in Ref. [12] but uses a different kinematic which takes into account the effect of the kink band angle β on the volume and transverse kink band stress which gives a more realistic stress state in the kink band at large deformations. The model incorporates the softening phase similar to other models but instead of a long constant plateau as in i.e. Ref. [23], the compressive stress increases again for large compressive strains. The model has been implemented in a commercial, explicit FE-code and is complemented by a criterion for kink band initiation and a mechanism for kink band broadening that allows the kink band to grow through the element at a constant stress during sustained crushing. Similar to the formulation in Ref. [23], no experimentally determined fracture toughness is necessary to fit the model but only the composite stiffness and the compression and shear strengths are required. The results presented in this paper illustrate the novelty of the proposed model in that it is capable of describing a chain of mechanisms including compressive failure initiation, initial softening due to kink band formation, a subsequent constant stress plateau at kink band broadening followed by a stiffening that leads to kinking initiation in adjacent finite elements. Combined these features of the model allows simulation of large compressive deformations without premature element deletion and thereby contributes significantly to the advancement of the simulation of constrained compression failure and crushing of composites.

2. Description of the kinking model

2.1. Implications of volume change due to kink band rotation

The geometry of a kink band is commonly defined in terms of inclination angle β and width w, see illustration in Fig. 1. Within the band, the fibres are rotated by an angle with regard to the fibre direction outside of the band. The maximum rotation angle, as measured e.g. in a test specimen after kinking failure, is called the lock-up angle $\widehat{\phi}$. For modelling purposes, the rotation angle is often divided into an initial misalignment angle $\overline{\phi}$ and a rotation due to loading ϕ, see illustration in Fig. 1. Many experimental studies have identified that the inclination angle β of the kink band is related to the lock up angle $\widehat{\phi}$ of the fibre rotation within the band, often measure after unloading as $\widehat{\phi} \approx 2\beta$ [13,24]. It has previously been proposed that the relation between β and $\widehat{\phi}$ can be explained via volumetric considerations [25] which, together with experimental observations, is the key motivation for that this relation has been used in modelling of kink bands [18,22]. To see this, consider the geometry of a section of a shear deformed kink band of length L_0 and height H in Fig. 2. The volume V of the kink band for a fibre rotation angle ϕ and an inclination angle β is

$$V = L_0 \cos(\phi - \beta) \frac{H}{\cos\beta}.$$

From this expression, it can be seen that the change of volume during kink band evolution (increasing ϕ) under planar deformation can be determined as

$$\frac{V}{V_0} - 1 = \frac{\cos(\phi - \beta)}{\cos\beta} - 1 = \varepsilon_1 + \varepsilon_2. \tag{1}$$

Here, ε_1 and ε_2 are the strains in and transverse to the fibre direction in the kink band, respectively. See also Fig. 2. With the assumption that the fibres are much stiffer than the matrix, the strain in the fibre direction is assumed negligible in comparison to the transverse strain, whereby Equation (1) reduces to

$$\frac{V}{V_0} - 1 = \frac{\cos(\phi - \beta)}{\cos\beta} - 1 = \varepsilon_2 \tag{2}$$

It can be noted that this expression for the transverse strain ε_2 is the engineering strain equivalent of the expression for the transverse strain in Ref. [12].

The transverse strain ε_2 from Equation (2) is plotted in Fig. 3 as function of kink band rotation angle for three different inclination angles β. For a β = 0, the transverse strain is always negative. For larger β angles, the transverse strain is first positive and then negative, being zero at $\phi = 2\beta$. For β values above 15–20°, the predicted maximum transverse strain is larger than the typical transverse failure strain of a UD lamina. This has been used by Matsou [14] to predict the variation of the β angle for samples tested in compression at a range of temperatures by using temperature dependent properties and stipulating that the lock-up angle is determined by transverse tensile failure in the kink band.

If the experimentally determined relation between rotation and inclination angles is due to volume effects, it could, as an extension, be argued that the rotation and inclination might develop simultaneously as the kink band progresses. This assumption has been used in Ref. [18] where it was also supported by experimental data showing that the end of the kink band had a shallower inclination angle and was less wide than the fully formed band. This is consistent with that the kink band propagates through a point in the material by initiation of kinking transverse to the main fibre direction, followed by rotation and widening of the kinked material as the band develops.

Although not conclusive from the literature, there are strong indications that the values of kink band inclination angle β and fibre rotation angle ϕ are coupled due to the volume effect discussed above.
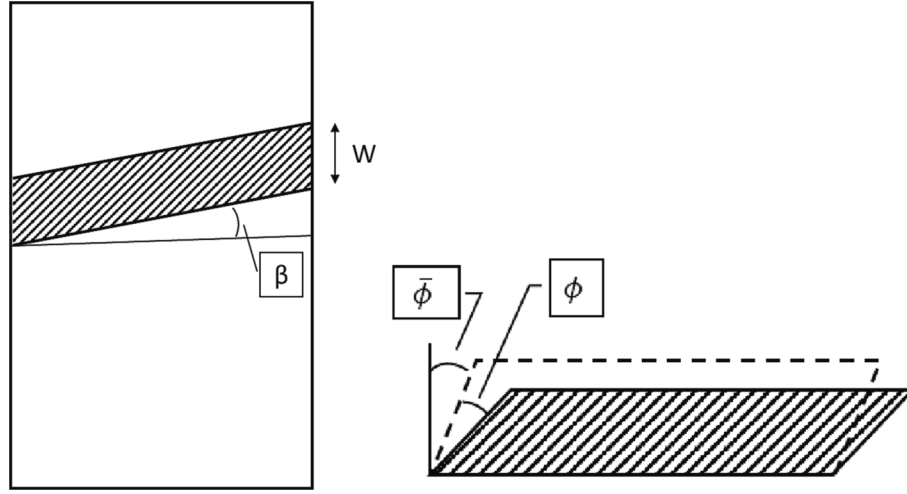
Fig. 1. Geometry of a kink band with inclination angle β and width w and illustration of fibre rotation angle ϕ within the kink band.
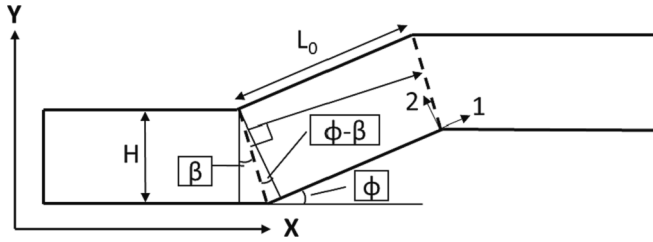

Fig. 2. Geometry for calculation of kink band volume.

The derivations above show that the fibre transverse stress and strain in the kink band are strongly related to the change in kink band volume, and hence in turn also to the values of angles β and ϕ. This will be utilized in the formulation of the kinematics of the equilibrium kink model as described in Section 2.3.

2.2. Equilibrium and displacement continuity conditions for a kink band

For a shear band, kink band or an embedded band with different material properties than the bulk material, equilibrium of tractions and continuity of the displacements over the interface are required, see Fig. 4. Specifically, it can be noted that continuity of displacement also requires that the stretching is continuous over the interface.

Equilibrium requires that the traction vectors over the interface are equal for the two materials, i.e. in terms of the stress tensors in the bulk and band material and with the use of the normal **n** from Fig. 5

$$\boldsymbol{n} * \boldsymbol{\sigma}^{bulk} = \boldsymbol{n} * \boldsymbol{\sigma}^{band} \tag{3}$$

Using the global coordinate frame and the geometry in Fig. 5, we introduce the band normal and the 2D matrix representation of the stress in the bulk and the band as

$$\boldsymbol{n} = (\cos\beta, \ \sin\beta), \ \boldsymbol{\sigma}^{bulk} = \begin{bmatrix} \sigma_X & \tau_{XY} \\ \tau_{XY} & \sigma_Y \end{bmatrix},$$
$$\boldsymbol{\sigma}^{band} = \begin{bmatrix} \widehat{\sigma_X} & \widehat{\tau_{XY}} \\ \widehat{\tau_{XY}} & \widehat{\sigma_Y} \end{bmatrix} \tag{4}$$

Which gives the two equilibrium equations

$$\cos\beta * \sigma_X + \sin\beta * \tau_{XY} = \cos\beta * \widehat{\sigma_X} + \sin\beta * \widehat{\tau_{XY}} \tag{5}$$

$$\cos\beta * \tau_{XY} + \sin\beta * \sigma_Y = \cos\beta * \widehat{\tau_{XY}} + \sin\beta * \widehat{\sigma_Y} \tag{6}$$
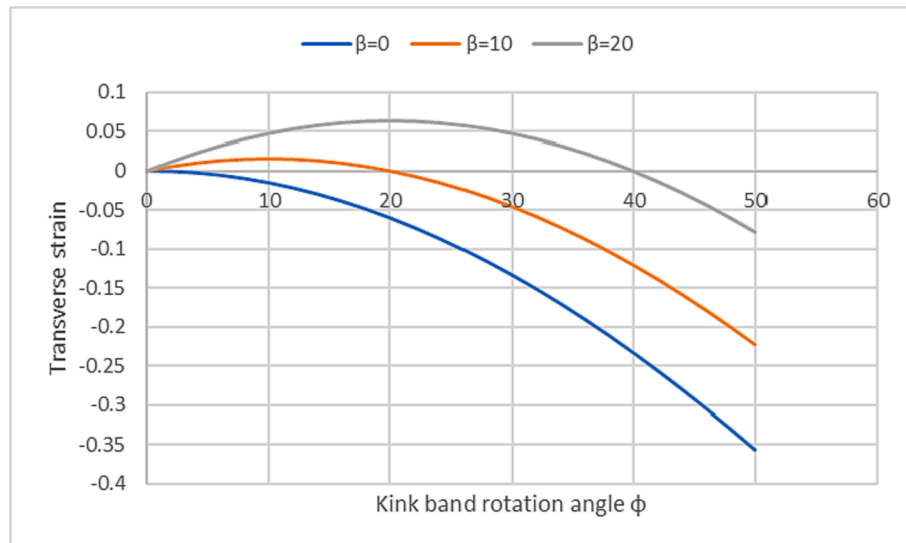

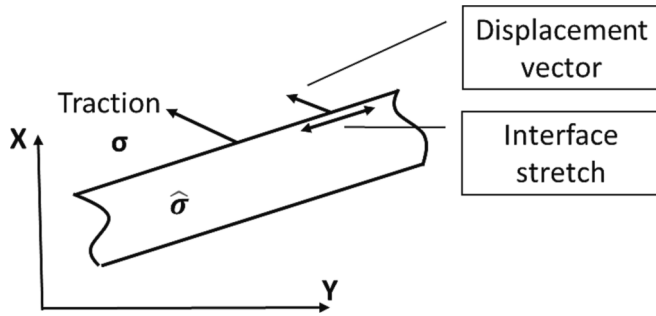**Fig. 3.** Transverse kink band strain as function of band rotation.

Fig. 4. Illustration of equilibrium and continuity conditions for an embedded band.
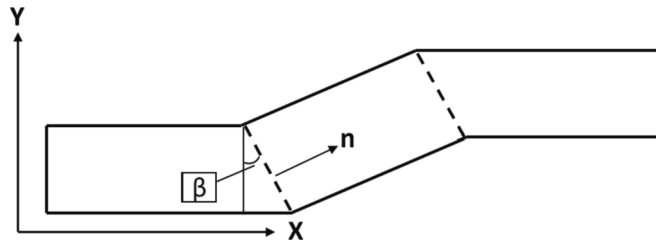

Fig. 5. Kink band geometry with interface normal used for stress equilibrium.

It can be noted that the stress tensors in the bulk and band are equivalent for $\beta \neq 0$ and $\sigma_Y = \widehat{\sigma_Y}$. Such an assumption would be logical for small fibre rotations where the global stiffness matrices for the two material states are very similar. For larger fibre rotations the correctness of such an assumption is more doubtful considering the equal stretch condition along the interface.

The large fibre rotation during kinking progression will give rise to a large axial compaction of the kink band (X-direction in Fig. 5) but also a simple shear type sliding as illustrated by the difference in Y direction displacement of the two sides of the kink band in Fig. 5. In a finite element setting, these kink band deformations, as well as the inclination angle β, can potentially be predicted using very detailed FE-models, see e.g. [26]. Another alternative would be to use a mesh size equal to the kink band width and model the case $\beta = 0$ geometrically. However, this would require including the effect of the β angle implicitly in the element kinematics in order to alleviate the volume effect on the local transverse strain. For larger element sizes more relevant for structural simulations, the kink band would need to be embedded within the element formulation. In this work is a smeared crack type model applied for this purpose. The sliding deformation from the fibre rotation is disregarded in the formulation for two reasons. Firstly, it simplifies the implementation greatly as only displacement compatibility between the bulk and kink band in the normal direction needs to be considered. Secondly, it reduces the risk for numerical issues due to large element deformations in combined compression and shear.

2.3. Derivation of kinking model based on equilibrium

In view of the discussion about volume changes in Section 1; if one considers the compressive failure process once initiated as a growth of the kink band into the undamaged region, the crucial aspect is the deformation state in the fully formed band. Naturally, in the transition zone from undamaged to kinked, the deformation and stress states are strongly influenced by e.g. the local flexibility around the kinking region. This is something that is challenging to describe. However, if one only considers possible end states when the band is fully formed and consider the angle β to take the value that is energetically the most favourable, one can see that the band can deform uncoupled from the

bulk deformation in both the normal direction of the band and in the direction transverse to rotated fibres. Given a constrained strain state, varying angles β can result in both compressive and tensile transverse stresses depending on the amount of fibre rotation, as evident from Equation (2) and in the results shown in Fig. 3.

For the equilibrium-based kinking model derived in this subsection, the following assumptions are made:

- The effect from the shear type sliding, as illustrated by the difference in Y-displacement between the bulk parts to the left and right of the kink band in Fig. 5, on the local stress and strain state in the bulk is not explicitly included in the formulation. Nevertheless, this does not automatically exclude the sliding effect to be incorporated on the FE-element level, even if this is not included in the current work.
- The global transverse stress in the bulk part and in the kink band are assumed equal.

The assumption of equal global transverse stress, i.e. $\sigma_Y = \widehat{\sigma_Y}$ in Equation (6), is based on the assumption that the kink band orients itself to fulfil this condition.

By assuming that the global transverse stress is equal in the bulk and in the kink band (i.e. $\sigma_Y = \widehat{\sigma_Y}$) in Equation (6), Equations (5) and (6) combined give that the stress tensors in the bulk and in the kink-band are equal for all values of β. This means that the stress state expressed in the kink band local fibre coordinate system is just obtained as the rotated bulk stress tensor:

$$\sigma_1 = \sigma_X \cos^2(\phi) + 2\tau_{XY} \sin(\phi)\cos(\phi), \tag{7}$$

$$\sigma_2 = \sigma_X \sin^2(\phi) - 2\tau_{XY} \sin(\phi)\cos(\phi), \tag{8}$$

$$\tau_{12} = -\sigma_X \sin(\phi)\cos(\phi) + \tau_{XY}\left(\cos(\phi)^2 - \sin(\phi)^2\right), \tag{9}$$

where 1, 2 are the local material axes of the kink band.

The axial kinking stress is, as in many other kinking models cf. e.g. [5,12,27,28], determined by the shear stress τ_{12} required for driving the rotation of the fibres in the kink band, see illustration in Fig. 6 and Equation (9). As the kinking induced shear strain is equal to the fibre rotation angle, and the shear stress is known through the constitutive behaviour, the kinking stress can be directly determined as function of fibre rotation angle from Equation (9). As the interest here is the composite behaviour at large rotation angles, beyond the strain levels
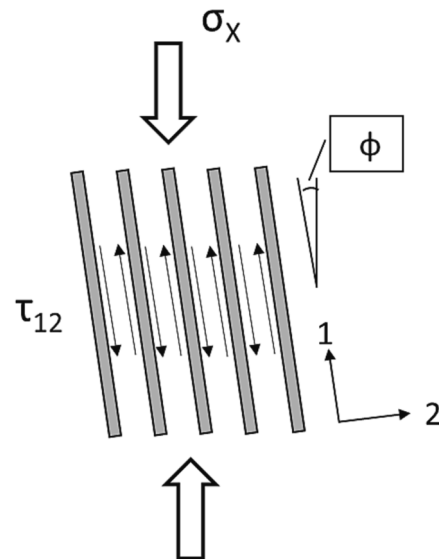

Fig. 6. Illustration of shear stresses necessary for equilibrium in off-axis UD composite under axial loading.

usually measured in shear tests, the shear stress is assumed to be constant (ideal plastic) at τ_{yield}. Hence, the model is suitable for rotation angles corresponding to shear strains above 5–10 %, see typical shear stress–strain curves in Refs. [8,29].

Generally, the hydrostatic pressure has an influence on the plastic stress–strain behaviour for polymers. Here, this is modelled by modifying the ideal plastic response to $\tau_{12} = \tau_{yield} - \mu\sigma_2$, where μ is a friction-like coefficient describing the influence of the transverse stress on the shear yield stress. The expression for the yield stress, together with Equation (9), allows the compressive kinking stress to be determined from the rotation angle and the bulk shear stress as

$$\sigma_X = \frac{\tau_{yield} - \tau_{XY}\left(cos(\phi)^2 - sin(\phi)^2 - 2\mu sin(\phi)cos(\phi)\right)}{\mu sin^2(\phi) - sin(\phi)cos(\phi)}. \tag{10}$$

2.4. Derivation of kinking model based on energy rates

In this subsection, an alternative kinking model is presented based on the requirement of balance between the power applied to the kink band and the strain energy rate within the same. Here, it is assumed that the strain energy rate in the band is dominated by the shear contribution. If the contribution to the strain energy rate from other stress–strain components is positive (i.e. no unloading), the compressive kinking stress predicted by the current model is the absolute minimum required to drive the fibre rotation.

Using the kinematics in Fig. 7, the displacement of the band interface in the fibre direction of the bulk part is

$$u = w((1 - cos(\overline{\phi} + \phi)) - (1 - cos(\overline{\phi}))), \tag{11}$$

After differentiation with respect to time, and multiplication with the compressive bulk stress σ_X^{ener}, the boundary power P is obtained as

$$P = \sigma_X^{ener} * \dot{u} = \sigma_X^{ener} * w * sin(\overline{\phi} + \phi)\dot{\phi} \tag{12}$$

The strain energy rate density due to the shearing from fibre rotation is constant through the band. By assuming that the shear strain is equal to the total fibre rotation, integrating over the band width w gives the strain energy rate E as

$$E = w * \tau_{12}\dot{\phi} \tag{13}$$

Now, equating the boundary power with the shear strain energy rate within the band (P = E), and rearranging terms, the compressive stress predicted from the energy rate balance is given by

$$\sigma_X^{ener} = \frac{\tau_{12}}{sin(\overline{\phi} + \phi)} \tag{14}$$

Note that as u is defined positive also the stress is defined as positive in compression and that, as for other kinking models, an initial imperfection is needed to avoid prediction of an infinite stress for zero rotation angle. For the current application, where only large rotation angles are considered and $\tau_{12} = \tau_{yield}$ is used, a split of the two rotation angles is not meaningful and only the sum is considered.

2.5. Kinking response results

In Fig. 8, the kinking stress–strain relations predicted by three different model configurations are shown for the case of a shear yield stress of 70 MPa; the energy rate kinking model from Section 2.4, the equilibrium kinking model from Section 2.3, and the equilibrium kinking model from Section 2.3 with an additional pressure coefficient of 0.30. The same data is plotted again in Fig. 9 but this time versus the compressive strain in the band. The compressive strain is a sum of the strain from the fibre rotation determined as u/w from equation (11), plus the elastic deformation due to compaction of the kink band in the local transverse direction, see Section 5.1 for details. The predicted kinking stress is similar for all three models at lower deformations which, considering the basis for the energy rate formulation, shows that the initial softening part is controlled by the stress required to drive the fibre rotation. For larger deformation the kinking stress from the energy rate model is slowly but continuously decreasing whereas the equilibrium models reach a plateau value and then start to increase. The increase in shear yield stress from the pressure coefficient leads to a higher plateau value at a lower shear angle. With a typical kink band inclination angle β of 20–25°, a shear angle (or fibre rotation angle) at lock-up of 40–50° is expected which is in the span of the plateau values for the two equilibrium predictions.

In addition, the local fibre and transverse stresses for the kinking model with pressure are plotted as function of the shear angle in Fig. 10. As can be expected, the transverse compressive stress increases and the compressive fibre stress decreases with increasing shear (or fibre rotation) angle. At around 60° shear angle, the axial stress increases sharply which causes the magnitude of the fibre stress to increase again. This displays that the chosen kinematic of the equilibrium model leads to a physical behaviour with the load increasingly carried by transverse compression as the fibre rotation angle increases, which in turn also means that a lock-up point can be predicted based on strength or when the surrounding material start to kink.

The results for the equilibrium model in Fig. 8 and Fig. 9 were generated for zero applied global shear stress. In Fig. 11, similar results are shown for the equilibrium model (no pressure dependence) for different levels of applied global shear stress. It is clear that, with the addition of the global shear stress, the curves are shifted towards lower shear angle values.

3. Kinking initiation

The kinking models described above are only valid for larger shear angles and need to be complemented with a kinking initiation criterion. Here, we adopt the original Budiansky-Fleck (B-F) model [12]. The B-F model is here used with two different sets of assumptions: (a) the angle β is zero and the transverse stress σ_t can be neglected, (b) the angle β is determined from that the transverse strain ε_t (and hence the volume change) is equal to zero, cf. setting the right hand side of Eq. (2) equal to zero. The latter also implies that the transverse stress is zero. For completeness, the Budiansky-Fleck kinking stress [12] is stated as function of shear stress τ_{12}, kink band angle β, imperfection angle $\overline{\phi}$, fibre rotation angle ϕ and applied global shear stress τ_{XY}, under the
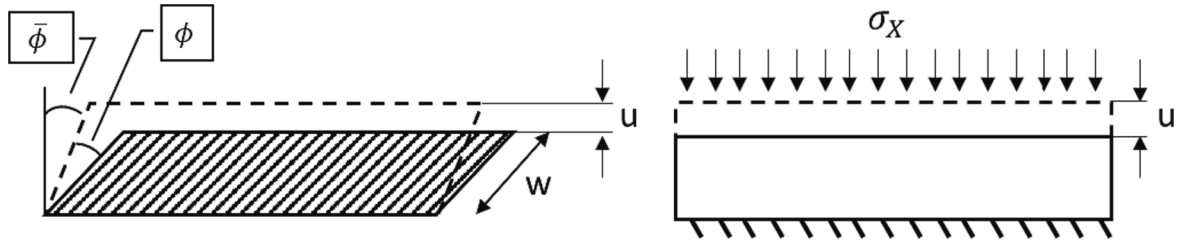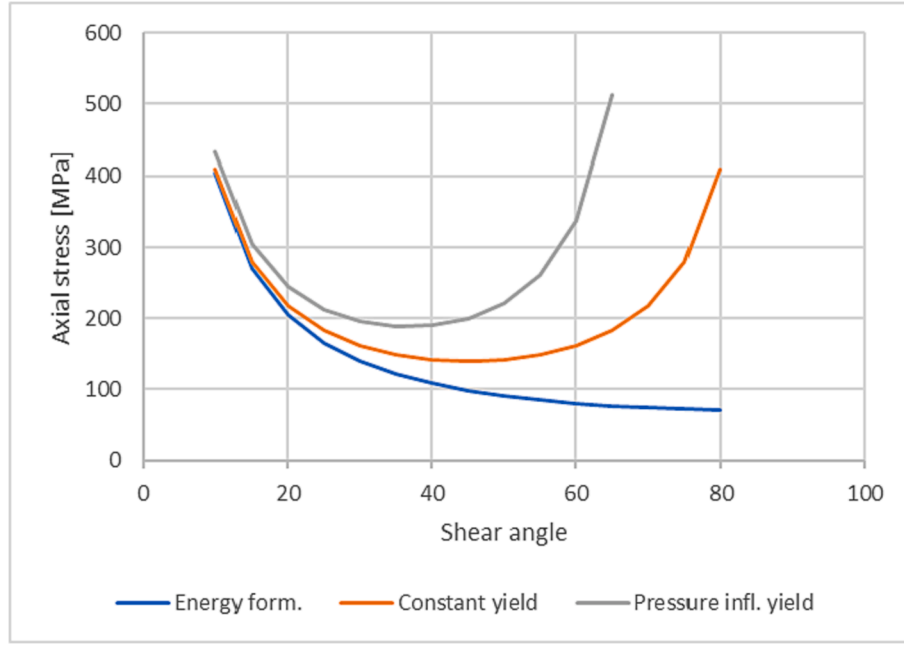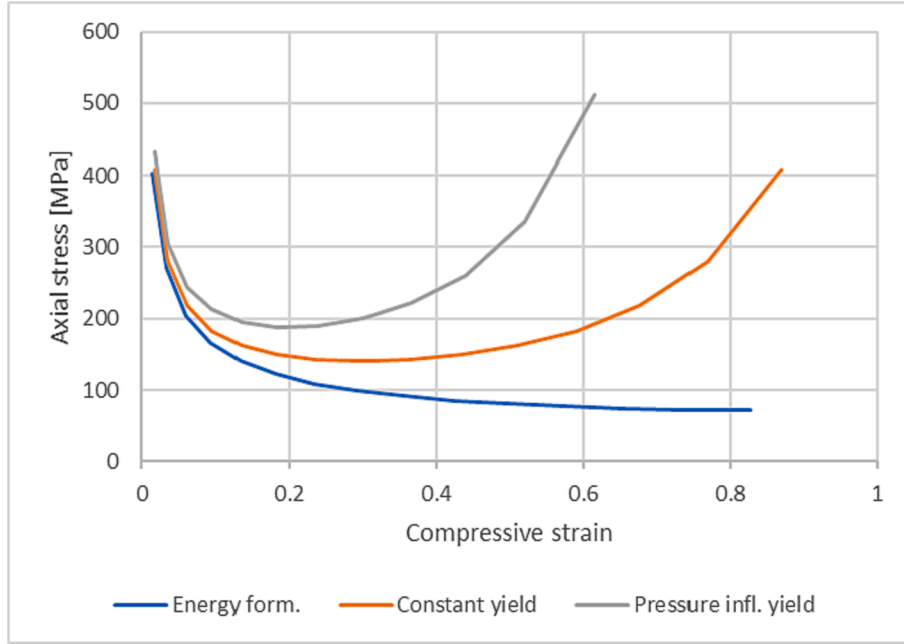

Fig. 7. Illustration of compressive deformation of kink band due to fibre rotation and kink band deformation u due to applied compressive load.

Fig. 8. Axial (kinking) stress as function of shear (fibre rotation) angle for the energy rate kinking model (Energy) and the equilibrium kinking model with μ = 0 (Constant) and μ = 0.30 (Pressure infl.) using a yield stress of 70 MPa.

Fig. 9. Axial (kinking) stress as function of compressive strain for the energy rate kinking model (Energy) and the equilibrium kinking model with μ = 0 (Constant) and μ = 0.30 (Pressure infl.) using a yield stress of 70 MPa.

condition $\sigma_t = 0$, as

$$\sigma_X^{B-F} = \frac{\tau_{12}cos(\beta - \overline{\phi} - \phi) - \tau_{XY}cos(\beta + \overline{\phi} + \phi)}{cos(\beta)sin(\overline{\phi} + \phi)} \quad (15)$$

Considering β, $\overline{\phi}$ and τ_{XY} as fixed parameters, the kinking stress can be determined as function of ϕ for a known constitutive relation $\tau_{12}(\phi)$. In this work, the shear stress–strain data from Ref. [29] are used, see Fig. 12. The kinking initiation stress is taken as the maximum value of σ_X^{B-F} with an initial imperfection angle of 3.6°. The latter was determined for the case of $\tau_{XY} = 0$ by calibration against the compressive

strength of 626 MPa obtained by Bru et al. [29].

How the predicted kinking initiation stress varies as function of global applied shear stress is presented in Fig. 13 for the two cases β = 0 and $\varepsilon_t = 0$. For comparison, a linear relation between compressive and shear strength, as used in Ref. [30] and in the LARC05 criterion applied in e.g. Ref. [9], is also included. Finally, the graph is complemented with the relation between kinking stress and applied shear stress for the equilibrium kinking model with μ = 0.30 at 10 % shear strain. As can be observed, the difference between the two assumptions for the Budinsky-Fleck model is small and the results are also close to the linear model.
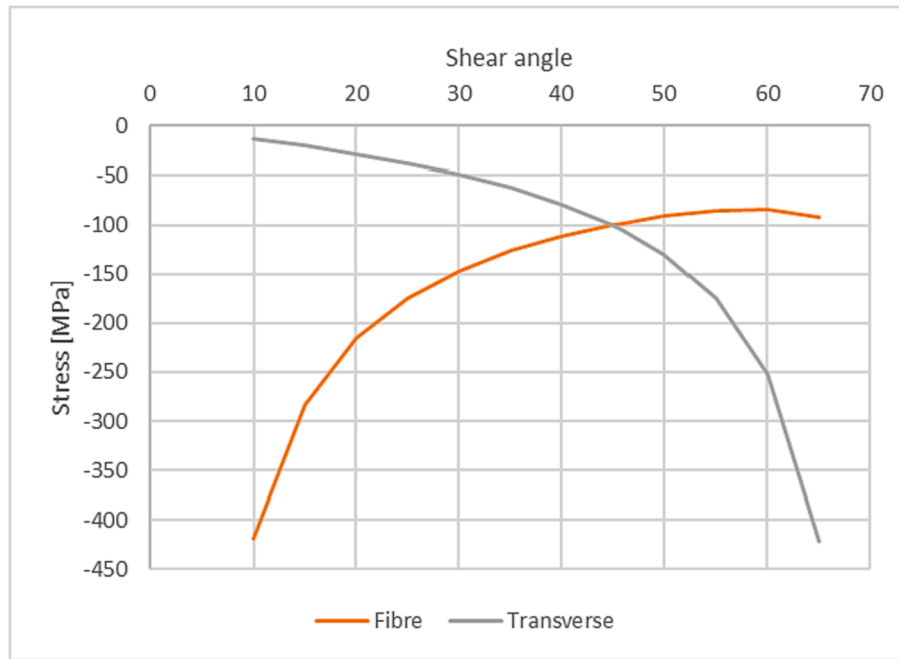
Fig. 10. Local fibre and transverse normal stress in the kink band as function of shear angle.
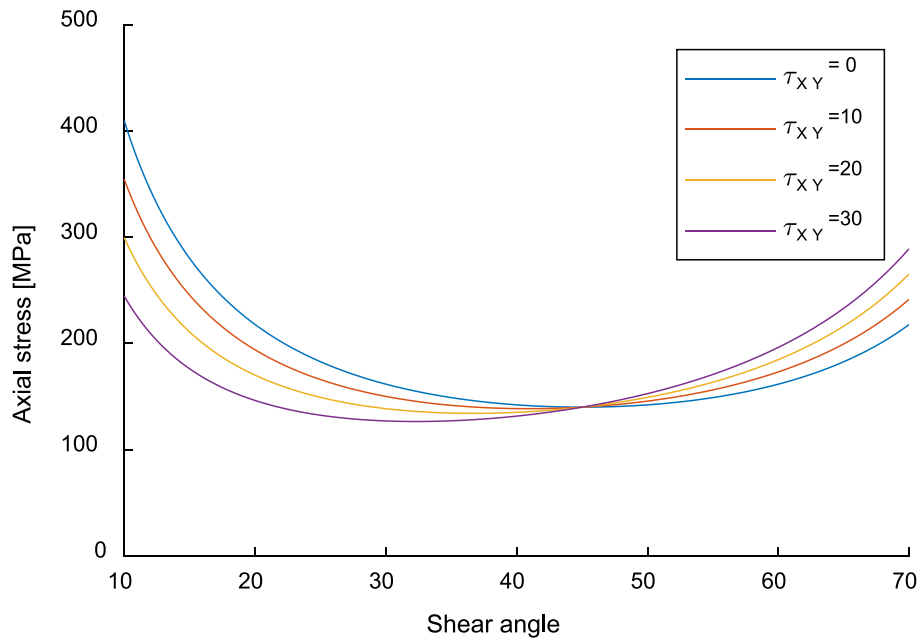

Fig. 11. Axial (kinking) stress as function of shear angle for $\mu = 0$ and different levels of global shear stress.

For higher shear stress values, the Budiansky-Fleck initiation stress is lower than the kinking stress from the equilibrium model. This can be explained by the pressure coefficient effect included in the equilibrium model but not in the Budinsky-Fleck formulation.

The fact that the Budinsky-Fleck initiation stress is lower than the kinking stress from the equilibrium model for large, applied shear stresses is an issue as the kinking stress would need to increase when the kink band is compressed from the initiation point to the compressive strain corresponding to 10 % shear strain. To assure that the kinking stress always initially decreases with increasing compressive strain, the initiation value is taken as the maximum between the Budinsky-Fleck model initiation stress or 110 % of the stress from the kinking model. The full kinking stress response as function of compressive strain in the

kink band is then obtained:

- From the kinking model for compressive strains corresponding to shear strains above 10 %
- Interpolated between the initiation stress and the kinking stress at shear strains below 10 %.

The resulting kinking stress curves for different applied global shear stress values are shown in Fig. 14.

4. Kink band broadening

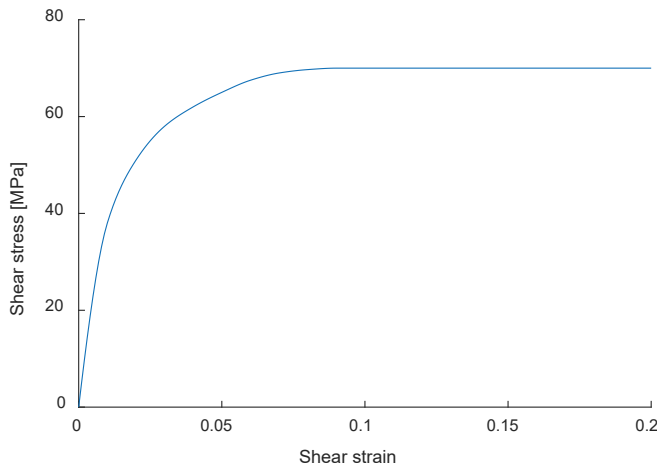From fractographic investigations, it is known that multiple kink

Fig. 12. Shear stress–strain curve used for the prediction of kinking initiation, data from Ref. [29].

bands can form on top of each other [15–17]. The term kink band broadening, first introduced in the work of [18,19] analysing the compressive failure of a IM7 carbon fibre PEEK material, describes this mechanism, where the width of a kink band grows under further loading in the post peak regime. In that work it was observed that due to the high strain to failure of the fibre, and the relatively small fibre rotation during kinking (attributable to the high strength matrix), the fibres in the kink band did not fail and the kink bands broadens by that the length of the straight part of the kinked fibres progressively grows. In about the same time, similar experiments were performed with carbon fibres with lower strain to failure [20,21] and a similar band broadening was identified. However, in this case the fibres break into multiple kink bands with practically constant width.

Expressions for the prediction of kink band broadening has been developed by both Budiansky and Fleck et al. [22] and Moran et al. [18]. Moran developed the model based on an energy balance between external load from the constant band broadening stress and the dissipation and stored elastic energy due to the shearing from fibre rotation.

To arrive at a closed form solution, an elastic–plastic law was applied based on a perfectly plastic response up to a certain shear strain, followed by a linear hardening at even higher strains. In Budiansky [22], a more elaborate way of formulating the problem using the principle of virtual work and including the effect of fibre bending, was shown to give the same result as an energy balance approach developed in the same paper. It can be noted that the energy balance approach by Budiansky in principle is equivalent to the approach by Moran and that it is used also here.

The external energy E_e from the constant band broadening at a stress σ_b is given as

$$E_e = \sigma_b * w * (1 - cos\phi) \tag{16}$$

The internally dissipated and stored energy comes from the local shear (dissipated) and transverse (stored) stresses and strains in the kink band. Assuming a homogenous state in the kink band gives

$$E_i = w * \left(\int_0^\theta \tau(\phi)d\phi + \sigma_2 * \frac{\varepsilon_2}{2} \right), \tag{17}$$

which allows the broadening stress to be calculated from

$$\sigma_b = \frac{\int_0^\theta \tau(\phi)d\phi + \sigma_2 * \varepsilon_2 \big/ 2}{1 - cos\phi}. \tag{18}$$

Here, the shear stress integral is evaluated using the stress strain curve in Fig. 12. The result is used together with the local transverse stress as shown in Fig. 10 and a transverse modulus E_2 = 9.15 GPa [29] to calculate the band broadening stress as function of max kink band rotation angle ϕ. The result is plotted in Fig. 15, together with the kinking stress for zero global shear stress. As the band broadening stress is the average stress required to grow the kink band, it should be determined based on the lock-up angle, i.e. the fibre rotation value at final failure of the composite. As the prediction of final failure is not included in the present work and experimental values for the kink band angle β is not available for the material in Ref. [29], a lock up angle of 45 degrees is assumed. This gives a band broadening stress of approximately 220 MPa.

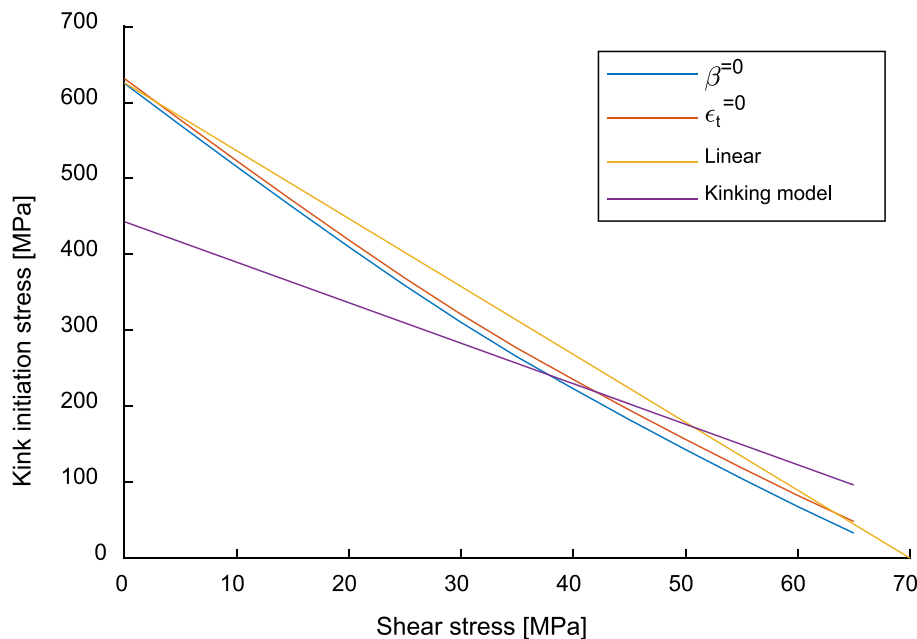The calculation here does, similarly to the Budiansky and Moran

Fig. 13. Prediction of kinking initiation using two variants of the Budiansky-Fleck model compared to a linear failure model and the stress from the kinking model at 10 % shear strain.
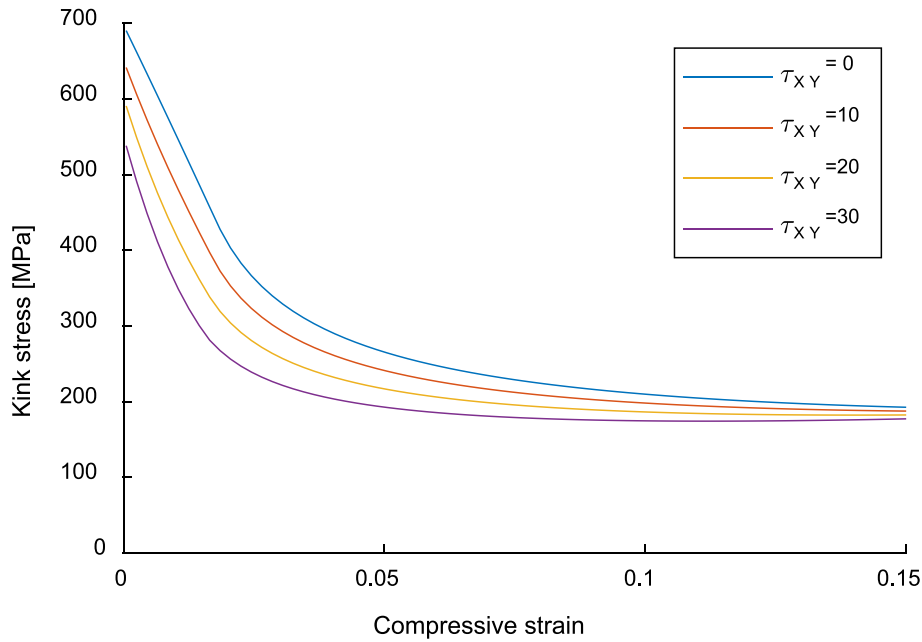
Fig. 14. Kink stress curves from the kinking model with values at lower strains interpolated from the initiation stress.
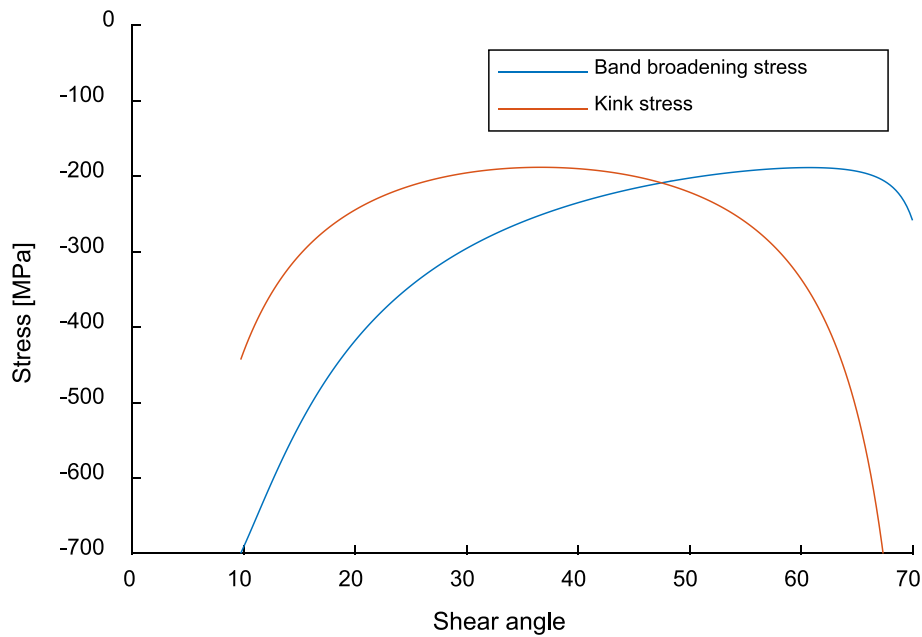

Fig. 15. Calculated band broadening stress as function of max fibre rotation angle during kinking and kink stress for zero global shear stress.

models, not consider fibre bending and fracture. However, the low fracture toughness of carbon fibres, typically in the order of 25–50 J/m^2 [31], means that fibre fracture energy is negligible compared to the toughness of kinking failure (magnitude of approximately 22–50 kJ/kg [6,29,32]) for realistic increases in kink width, unless additional large plastic dissipation occurs during the fibre fracture process. It can be noted that the current model predicts a fracture toughness of 29 kJ/m^2 for 0.4 mm kink band width when the global shear stress is assumed to be zero.

5. Finite element implementation

5.1. Strain decomposition and stress degradation

The equilibrium-based kinking model is to be implemented as a user material in the explicit FE-code Ls-Dyna. To facilitate the implementation in a 3D stress and strain setting, the kinking model needs to be integrated with a standard, orthotropic constitutive model in a smeared crack type formulation. To facilitate the combination of an elastic orthotropic response next to the kink band with that of a softening response within the kink band, the element strain in the fibre direction is decomposed into one elastic part (for the surrounding bulk material) and one kink band part. The decomposition is based on the relation between the kink band width and the element length in the direction

perpendicular to the kink band orientation, see illustration in Fig. 16. This requires a few simplifying assumptions to be made for the implementation that are in-line with the assumptions made earlier for the kinking model, see Section 2.3.

In the equilibrium model the stress state in the kink band is the same as in the bulk part. The implementation here is done for β = 0 geometrically and the continuity of the stretch gives that also the transverse strain is equal in the kink band and in the bulk. Moreover, the shear deformation in the bulk due to the shear type sliding deformation over the kink band is neglected, see Fig. 5 and Section 2.3. This implies that the shear deformation is assumed unaltered by the introduction of the kink band and consequently that the shear strain is equal in the bulk and in the kink band.

Within the context of implementation, any direction reference is made with regard to the lamina (bulk) when not explicitly stated. Also, standard notation of 1, 2, 3 for fibre, transverse and through thickness direction respectively are used. The fibre kinking can be both in-plane and in the through thickness direction depending on the material structure (e.g. waviness) and loading [33]. This is considered in the model by that the combined magnitude of the in-plane and through thickness shear stresses is used for the prediction of kinking:

$$\tau^{kink} = \sqrt{\tau_{12}^2 + \tau_{13}^2} \tag{19}$$

Consequently, the transverse and through thickness directions are treated alike and the only strain that is different in the bulk and in the kink band is in the fibre direction.

The kink band model is one dimensional in that it gives a prediction of the compressive stress in the 1-direction from the compaction of the kink band. However, a generalisation of the formulation to a 3D state needs to consider that the stress in the fibre direction is influenced not only by the fibre strain but also by the transverse and through-thickness strains. However, if the influence on the kinking process from the transverse and through-thickness strains can be neglected, the evaluation of the non-linear response can be simplified. With this in mind, the stress strain relation is written as

$$\boldsymbol{\sigma} = \boldsymbol{d} \bullet \boldsymbol{C} \bullet \boldsymbol{\epsilon}, \tag{20}$$

where **C** is the linear elastic stiffness matrix for the lamina, ∈ is the average strain vector as determined from the deformation gradient and **d** is a damage type matrix with

$$\begin{aligned} d_{11} &= 1 - d\big(\epsilon_{11}, \tau^{kink}\big); \\ d_{ii} &= 1 (i \neq 1); \quad d_{ij} = o (i \neq j). \end{aligned} \tag{21}$$

Here, ϵ_{11} is the strain component in the fibre direction. The component d_{11} is introduced to reduce the elastic stiffness in the fibre direction such
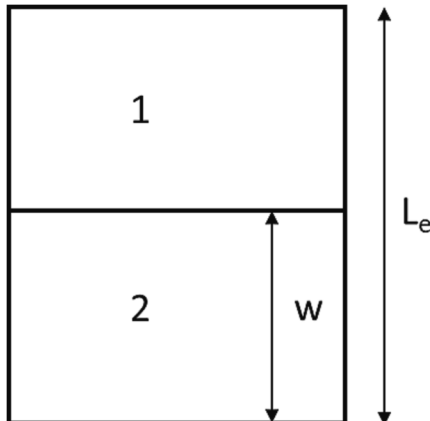

Fig. 16. Division of structure into two areas (1) bulk and (2) kink band.

that the resulting compressive stress equals the kinking stress. Using the kinking model in Eq. (10) together with the global shear stress from Eq. (19), an expression for the kinking stress (with a different nomenclature) is obtained as:

$$\sigma_{kink} = \frac{\tau_{yield} - \tau^{kink}\big(cos(\phi)^2 - sin(\phi)^2 - 2\mu sin(\phi)cos(\phi)\big)}{\mu sin^2(\phi) - sin(\phi)cos(\phi)}, \tag{22}$$

whereby the damage type factor d_{11} (21) can be calculated as

$$1 - d_{11} = \frac{\sigma_{kink}}{\sigma_{11}^{el}}. \tag{23}$$

Here, σ_{11}^{el} is the elastic stress determined for uniaxial straining using the compressive strain in the kink band. Note that as the kinking model is assumed to be 1D, the simplification of uniaxial stress and strain is used throughout to calculate the stress and strain measures for the strain decomposition and the determination of d_{11}.

To decompose the compressive strain, we first note that the total deformation of the kink band in the bulk fibre direction is caused by a combination of a contribution from the rigid fibre rotation

$$\varepsilon_{rot}^{kink} = 1 - cos(\phi) \tag{24}$$

and a contribution from the compression of the kink band ($\varepsilon_{comp}^{kink}$). To determine the latter, we first note that the elastic strains in the kink band local material system can be calculated from the local stresses in Eqs. (7) and (8) as

$$\begin{aligned} \varepsilon_1^{kink} &= S_{11} {}^* \sigma_1^{kink} + S_{12} {}^* \sigma_2^{kink}, \\ \varepsilon_2^{kink} &= S_{21} {}^* \sigma_1^{kink} + S_{22} {}^* \sigma_2^{kink}, \end{aligned} \tag{25}$$

where S_{ij} are components of the compliance matrix. Here, it should be noted that the assumption is that the compression after the rotation does not introduce any extra shear deformations, but that these are already included in the rotation.

The added straining in the bulk fibre direction, coming from the local strains in the kink band, is then calculated from the regular strain transformation equations as

$$\varepsilon_{comp}^{kink} = \varepsilon_1^{kink} cos(\phi)^2 + \varepsilon_2^{kink} sin(\phi)^2, \tag{26}$$

and the total strain in the kink band is obtained from

$$\varepsilon_{tot}^{kink} = \varepsilon_{rot}^{kink} + \varepsilon_{comp}^{kink}. \tag{27}$$

For the decomposition of the strain in the fibre direction, a division into two element layers is used as shown in Fig. 16, the bulk layer (1) and the kink layer (2). The other nomenclature shown in Fig. 16 is the height of one kink band w and the element length in the fibre direction L_e

The average strain, which is the elemental strain in the 1 direction, can be written as

$$\varepsilon_{11}^{av} = \varepsilon_{11}^{bulk}\left(1 - \frac{w}{L_e}\right) + \varepsilon_{tot}^{kink}\frac{w}{L_e}, \tag{28}$$

with the bulk strain from

$$\varepsilon_{11}^{bulk} = \frac{\sigma_{11}^{kink}}{C_{11}}, \tag{29}$$

where C_{11} is the 11 component of the stiffness matrix **C**.

The kinking stress can then be easily calculated from Eq. (22), and the average compressive strain from Equations (24) to (29) for known values of fibre rotation angle and global shear stress. In the implementation, however, the average strain is known and the kinking stress that gives the correct average of bulk and kink band strains need to be found. In practice, this means to determine the rotation angle. As an analytical solution is difficult to find, and although it's possible to

numerically iterate to find the rotation angle, an interpolation procedure is applied here for efficiency and convenience. To do so, first a set of piecewise linear curves, describing the relation between σ_{kink} and ε_{tot}^{kink}, are generated from a range of fibre rotation angles and global shear stresses using Eq. (22) and Equations (24) to (29). Also, as will be evident later, values of the stiffness related to the $\varepsilon_{comp}^{kink}$ strain

$$C_{11}^{kink} = \sigma_{kink} \Big/ \varepsilon_{comp}^{kink} \qquad (30)$$

will be required. Therefore, a set of piecewise linear curves with C_{11}^{kink} versus ε_{tot}^{kink} is also generated in a similar fashion.

With the use of linear interpolation, the kinking stress between two strain points can be written as

$$\sigma_{11}^{kink} = K_1 + K_2 * \varepsilon_{tot}^{kink}, \qquad (31)$$

with the constants K_1 and K_2 being determined from fitting Eq. (31) to two $\sigma_{11}^{kink}, \varepsilon_{tot}^{kink}$ pairs of the piecewise linear curve. Solving for ε_{tot}^{kink} from Eq. (31), and using the result together with Eq. (29) in Eq. (28), allows the kinking stress to be calculated as

$$\sigma_{11}^{kink} = \frac{\varepsilon_{11}^{av} + \frac{K_1 w}{K_2 L_e}}{\frac{1}{C_{11}}\left(1 - \frac{w}{L_e}\right) + \frac{w}{K_2 L_e}} = \frac{\varepsilon_{11}^{av}\frac{L_e}{w} + \frac{K_1}{K_2}}{\frac{1}{C_{11}}\left(\frac{L_e}{w} - 1\right) + \frac{1}{K_2}}. \qquad (32)$$

In practice, the implementation requires a possibility to iterate, as σ_{11}^{kink} determined using the interpolation needs to be between the stress values of the two $\sigma_{11}^{kink}, \varepsilon_{tot}^{kink}$ pairs used for the determination of K_1 and K_2. For this iteration, it can be noted that the value of ε_{tot}^{kink} is bounded by the cases of i) equal strain in bulk and kink band ($\varepsilon_{tot}^{kink} = \varepsilon_{av}$) and ii) all strain localised to the kink band ($\varepsilon_{tot}^{kink} = \varepsilon_{av} \bullet L_e/w$). Thereby, these two bounds can be used as upper and lower limits on the strain during the iteration to determine the kinking stress.

As a final note, we emphasise that kinking failure will lead to large values of ε_{11}^{av}, and consequently also to an unwanted, large impact on the transverse and through thickness stresses through the 12 and 13 terms of the stiffness matrix C. This happens since only the stress in the fibre direction is reduced by d in Eq. (20). To correct for this, an elastic strain, corresponding to the compressive stress, is used to determine the transverse and through-thickness stresses using the relation in Eq. (20). In line with the 1D calculation of the damage variable d_{11}, this elastic strain is determined as

$$\epsilon_{11}^{el} = \varepsilon_{11}^{bulk}\left(1 - \frac{w}{L_e}\right) + \varepsilon_{comp}^{kink}\frac{w}{L_e} = \frac{\sigma_{11}^{kink}}{C_{11}}\left(1 - \frac{w}{L_e}\right) + \frac{\sigma_{11}^{kink}}{C_{11}^{kink}}\frac{w}{L_e}. \qquad (33)$$

Here, it is also noted that, during kink band broadening the kinking stress is constant and hence also ε_{tot}^{kink} and the increase in kink width w can be directly determined from Eq. (28) using $\sigma_{11}^{kink} = \sigma_b$.

5.2. Large deformation effects

In the derivation above, the stress and strain measures are the engineering (small) stress and strain. However, for the implementation in LS-Dyna the Second Piola Kirchoff stress S and the Green Lagrange strains are used to accommodate for larger deformations. As a consequence, due to the large compressive deformation during kinking, the difference between the two sets of stress and strain measures needs to be compensated for in order to get the intended kinking response.

To do so, we first note that the kinking response based on the strain decomposition in Eq. (32) actually is determined by the total deformation over the kink band, even though it is expressed in terms of engineering strain. With a direct use of Green Lagrange strains, the expressions in Eq. (24) and Eq. (28), along with others, are no longer representative of the kink band kinematics. This is explained by that

these expressions are derived based on the total displacement over a certain distance, i.e. the kink band width or element height. As it is generally not possible to calculate engineering strains directly from Green Lagrange strains, the engineering strains need to be estimated. To do so, it is assumed that only the strain in the fibre directions is large (all other strain components are small), whereby an estimate of the engineering strains to be used can be made based on (nearly) uniaxial deformation. By using the definition of engineering and GL-strain for a uniaxial displacement u in the direction of X, an approximation of the engineering quantity is obtained as:

$$\varepsilon_{11} = \frac{du}{dX}; GL_{11} = \frac{du}{dX} + \frac{1}{2}\left(\frac{du}{dX}\right)^2; \varepsilon_{11} = \frac{du}{dX} = -1 + \sqrt{1 + 2*GL_{11}}. \qquad (34)$$

To clarify, the expression in Eq. (34) is used to estimate ε_{11} used in the kinking evaluation from GL_{11}.

Further, in this work the engineering stress is interpreted as the First Piola Kirchoff stress P, which is related to the second Piola Kirchoff stress S through the deformation gradient as

$$P = F \bullet S \qquad (35)$$

Clearly, there is a difference between the stress measures for large material stretches as e.g. for the compressive deformations seen during kinking. As once more the intended kinking response is defined in terms of the engineering quantity (here interpreted as P), the kinking stress needs to be properly scaled with the deformation to obtain the correct second Piola Kirchoff stress S as output from the model. Using Equation (35), together with the requirement that the scaled second Piola Kirchoff stress component $\hat{S}_{11}$ in the kinking direction should give the correct first Piola Kirchoff stress component P_{11} for a uniaxial kink deformation, gives

$$P_{11} = \hat{S}_{11}\left(1 + \frac{du}{dx}\right) \underset{\Rightarrow_{11}}{\hat{S}} = P_{11}\Big/(1 + e_{11}) \qquad (36)$$

In practice this is used in the calculation of the damage type variable d_{11} introduced in (21) to end up at

$$d_{11} = \frac{\sigma_{11}^{kink}}{C_{11} \bullet GL_{11} \bullet (1 + e_{11})} \qquad (37)$$

An illustration of the schematic for the subroutine implementation is shown in Fig. 17.

5.3. Ls-Dyna implementation and input data

The kinking model as described above has been implemented as a user material in the explicit FE-code Ls-Dyna. Model parameters as the material stiffness properties for the bulk lamina, the broadening stress limit σ_b and the initial kink band width w are input in the user material deck. Other necessary data are input as curves: The kink initiation stress and the strain and axial stiffness at start of band broadening are input as function of the global shear stress. The kinking stress and stiffness are input as function of total kinking strain with separate curves for different levels of global shear stress.

In Fig. 18 the stress–strain behaviour for a single element test is shown for a 1 mm element with an initial kink band width of 0.6 mm, a band broadening stress of 220 MPa and an applied shear stress of 10 MPa. The strain used in the plot is the engineering compressive strain calculated from the element displacement. Similarly, the stress is determined from the reaction forces of the element nodes. In Fig. 18 are the stages in the kinking evolution indicated. After the initial, elastic response and initiation of kinking (Eq. (15) there is a softening phase ending with a plateau and a slight upturn (Eq. (22)). When the kink stress has increased to the kink band broadening limit, the upturn is interrupted and the stress is constant while the width w of the kink band increases (Eq. (28)) until it spans the full element. Finally, the stiffness of
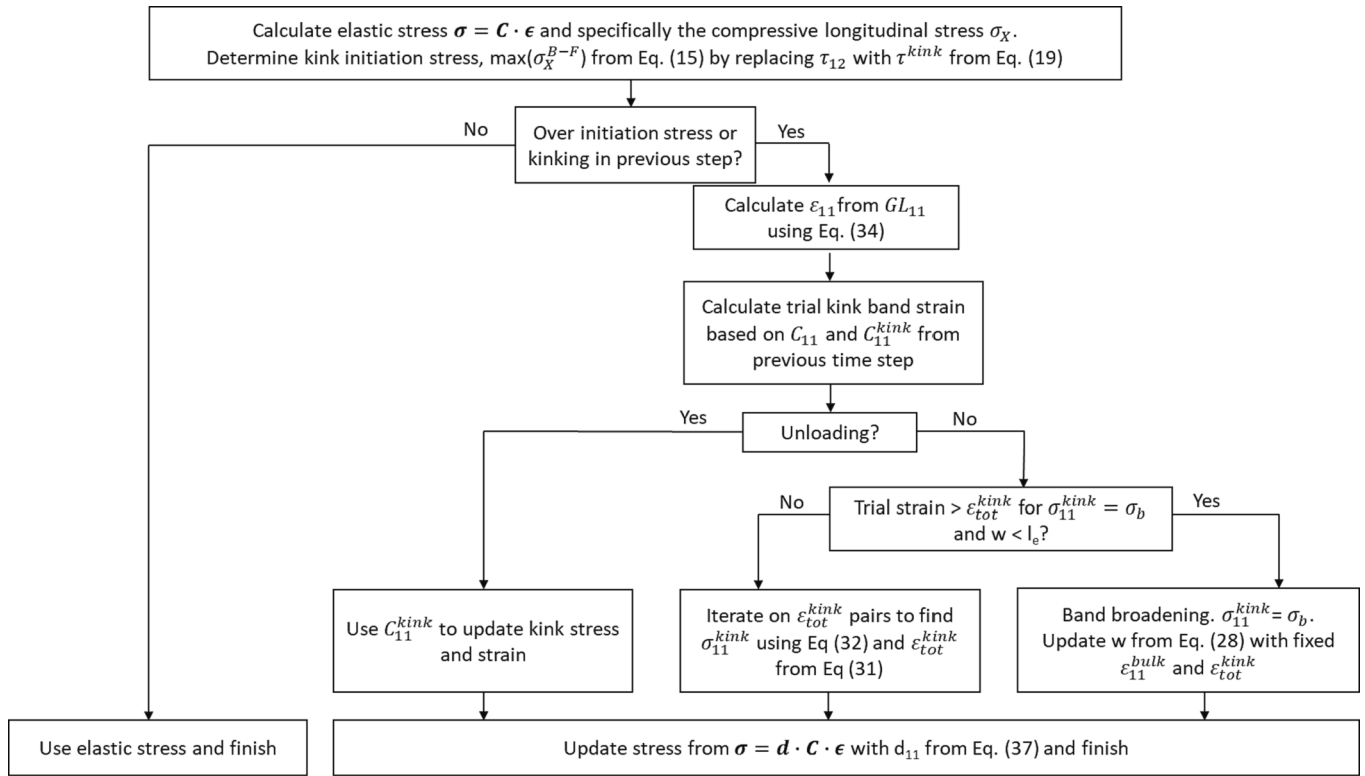
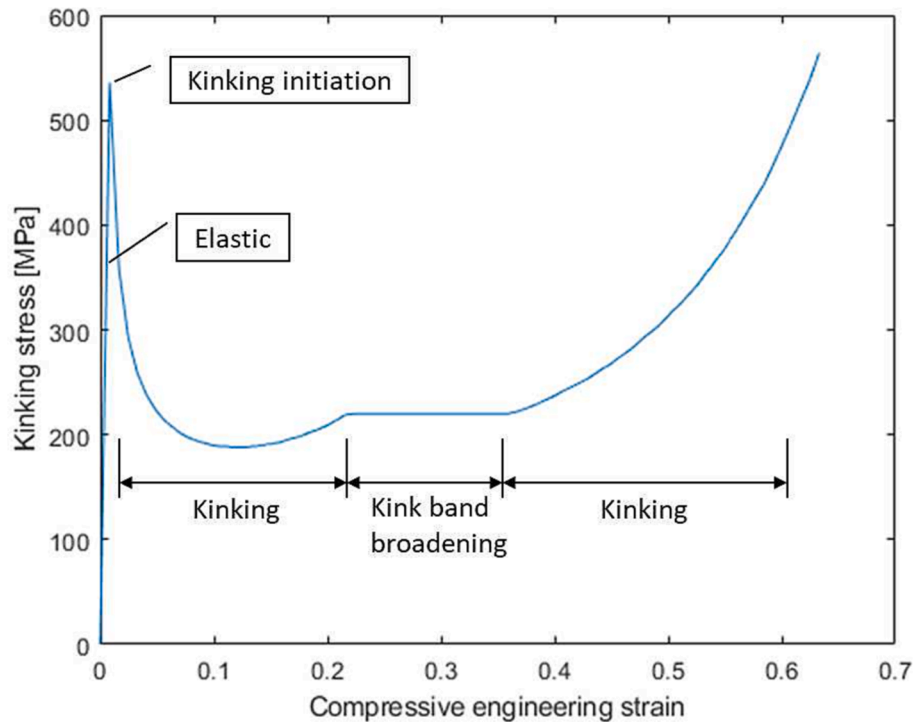**Fig. 17.** Illustration of the schematic for the subroutine implementation.

Fig. 18. Stress–strain response for compressive deformation of a single 1 mm high element with a 0.6 mm wide kink band.

the kink band increases substantially as kinking continues and when the element is compressed by ~60 % the stress level is back to the kink initiation level so that the kinking potentially could be initiated in a neighbouring element.

6. Results

6.1. Compression test example

A simple compression analysis is used to evaluate the performance of the kinking model including sustained crushing stress and stiffening as

well as the influence of different element sizes. The dog-bone shape of the compression specimen used for the analysis has dimensions as shown in Fig. 19. The thickness is 2 mm. It is emphasised that this geometry is not based on test standards but rather used to illustrate the behaviour of the model.

The dog-bone is discretised with standard first order continuum elements using two different mesh sizes: 0.6 and 1.2 mm also resulting in 4 and 2 elements through the thickness, respectively. The mesh with smaller elements is shown in Fig. 19.

The elastic material properties and the kink band properties for the UD ply are shown in Table 1 where μ is the pressure coefficient, σ_b is the broadening stress, $\overline{\phi}$ is the imperfection angle for the kinking initiation and X_c is the compressive strength of the ply. All properties are taken from Ref. [29] except μ and σ_b. σ_b is calculated from Eq. (18) as described in Section 4 and μ is estimated from that the yield plateau increases in the same way with normal stress as the shear strength. The value is obtained from the recommendations for carbon/epoxy composites in Ref. [34]. A kink band width of 0.3 mm is specified based on the fractographic pictures in Ref. [35] where the same composite material is in Ref. [29] was used.

The loading of the compression specimen is defined in terms of a prescribed velocity of the upper edge of the specimen, using a slow sinusoidal ramp-up to get a smooth increase in stress and strain before failure initiation. During the velocity ramp up, also a small rotation is applied to the upper edge in order to give a small but nearly constant difference in strain between the two sides of the specimen. The applied rotation is constructed such that the axial strain at the right side is approximately 10 % higher than at the left side at initial failure of the specimen. The lower edge of the specimen is fully constrained in all three directions.

The reaction force versus applied edge displacement response is shown for the two different meshes in Fig. 20. No filtering has been applied to the results. A linear response is seen up to kink band failure initiation, where a kink band initiates at the side with the slightly higher axial strain. This kink band then quickly propagates through the width of the specimen during the load drop as shown in Fig. 21. The sudden load drop seen after kind band initiation leads to an unstable, dynamic response before the load stabilises and thereafter starts to gradually increase again during the kink band evolution. The plateau just below 6 kN corresponds to the steady crushing during the kink band broadening followed by stiffening when the kink band spans the full element height.

In Fig. 22 is the specimen shown just before (left) and just after (right) the second load peak in Fig. 20. The left specimen contains a single row of compressed elements with kink bands whereas the specimen to the right also has a full second row of elements containing kink bands. Upon further loading the strain field is no longer homogenous across the width, whereby a new kink band initiates at a lower reaction force. The subsequent kinking failure progress that follows is then unstable, as shown in Fig. 23. From the results shown in Fig. 20, the response of the 1.2 mm model is very similar. Failure initiates at the same point, the plateau corresponding to the kink band broadening is longer as the kink band widens from 0.3 to 1.2 mm rather than to 0.6. In contrast to the 0.6 mm model, the kinking failure in the 1.2 mm model grows into the radius of the specimen and consequently displays a lower force level at the second peak due to a less homogenous strain field. After the third load peak the kink band failure is unstable also in the 1.2 mm model.

6.2. Flexure test example

Unfortunately, there are no data available from flexural tests with UD lay-up for the material used to calibrate the current kinking model. Similarly, we have no access to the necessary shear stress – shear strain data to calibrate the model for another material system for which flexural test data exists. Therefore, no direct comparison can be made to experimental results. The model results presented here are instead comparing general features observed in flexure testing of other carbon fibre-epoxy systems.

Due to the lower strain to failure in compression compared to tension, a strength analysis in bending will predict failure on the compressive side. However, flexure specimens are often reported to fail in tension and at loads considerably higher than simulation predicted failure loads. As an example, the FE-analysis of a 4-point flexure test in Ref. [36] underpredicted the failure load by 17 %. Furthermore, even though the model predicted a compressive failure, the experimental results showed tensile failure below the loading points. Furthermore, Burgani [37] analysed 3-point bending test data from the literature using FE simulations with different strength criteria. The Tsai-Wu criterion showed the best correlation with experimental test data, underpredicting the failure load with 6 %, 9 % and 14 % for the three different material systems. This despite that the compressive stress component at failure was 9 %, 25 % and 10.5 % above the fibre compressive strength, explained by the interaction between fibre and transverse stresses in the Tsai-Wu criterion. In addition, [38] used a 4-point flexure set-up to study the effect of thickness on strain to failure. All geometrical dimensions except for the width, but including the rig and load cylinder diameter, were scaled two and four times. For the two lower thicknesses the failure was in tension, whereas the 4 times scaled specimen failed in compression under the loading points. A similar result was seen in the 3-point flexure results in Ref. [39] where a transition from tensile to compressive failure could be seen when moving from 2 to 4 mm thickness up to 6–7 mm.

Here, the 4-point flexure set-up used in the simulation are based on the geometry used in Ref. [38], see Fig. 24, the lay-up is UD with the fibres oriented in the beam length direction. The 5 mm specimen width in the FE-model is half of that of the test specimen (10 mm), employing symmetry constraints along the symmetry plane. The 1 mm thick rubber pads used in the original experiments between the specimen and the loading cylinders are modelled with a linear material with Young's modulus 200 MPa and a Poisson's ratio of 0.40. The composite properties used are the same as in the previous example, so is also the base kink band width of 0.3 mm and the element length of 0.6 mm. The element height used is 0.3 mm as a trade-off between resolution and element aspect ratio for the 1-point integration solid element formulation used. Contact conditions are applied both between the rubber pads and the specimen and between the pads and the rigid shells representing the loading cylinders. Note that the thickness applied to the rigid shells is considered in the contact formulation and that the shells therefore are
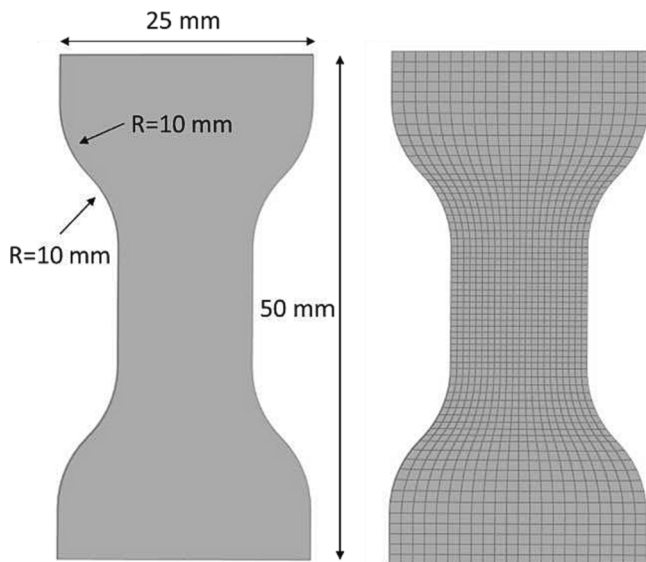

Fig. 19. Geometry and dimensions of compression specimen and the 0.6 mm mesh. The thickness is 2 mm and with 4 elements through the thickness.

Table 1

Elastic and kinking model properties used for the UD-ply [29].

Elastic ply properties								
E_1 [GPa]	E_2 [GPa]	E_3 [GPa]	ν_{12}	ν_{13}	ν_{23}	G_{12} [GPa]	G_{23} [GPa]	G_{31} [GPa]
136	9.15	7.7	0.28	0.35	0.36	4.4	3.7	3.018
Kinking model and failure properties								
τ_{yield} [MPa]	μ^*	$\sigma_b{}^*$ [MPa]	$\overline{\phi}$ °	X_c [MPa]				
70	0.30	220	3.6	626				

* Estimated or calculated property.
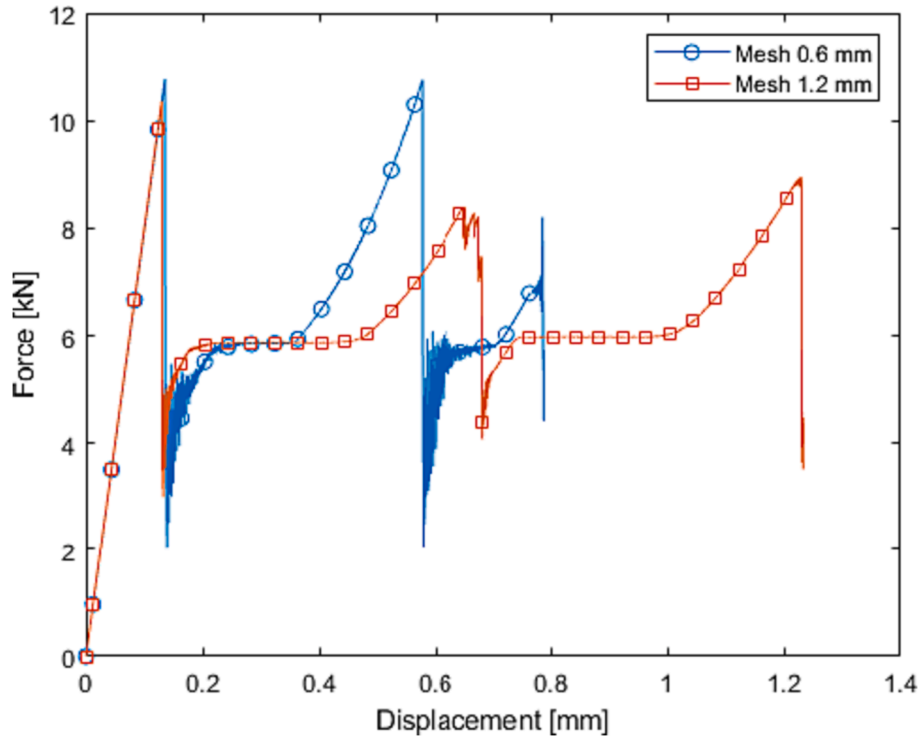
Fig. 20. Force versus displacement for compression specimens with mesh 0.6 mm and 1.2 mm.

offset w.r.t. the pads in Fig. 24 and the following result plots. The loads are defined in terms of a prescribed velocity with a slow, sinusoidal ramp-up applied to the top loading cylinders, while the lower ones are fixed. It was verified that the chosen loading rate was slow enough so that no dynamic effects could be seen on the stress and strain distributions before failure.

Results presented in the following are for the base model as described above, the same model but with a kink band width of 0.15 mm and a model with all dimensions scaled 4 times. For the latter, the mesh size is left unchanged, while the applied velocity is scaled 4 times to keep the approximate time to failure load unchanged. In all models (also the scaled), one of the lower supports is moved 5 mm inwards to disturb the symmetry and prevent simultaneous failure on both sides.

In Fig. 25, the load versus displacement of the centre of specimen is shown for the three models. It can be noted that the scaled specimen is less stiff in the initial part, which is explained by the somewhat longer span due to the 5 mm in-wards displacement of one support in all models. Comparing the model with reduced kink width to the base model, compressive failure is initiated at the same applied displacement but the fact that the softening at kinking takes place over a shorter displacement leads to a larger first load drop. For the scaled specimen, the load at initiation is lower than for the base model. This is explained

by that the upper-most integration point is in relative measures closer to the surface (absolute distance is 0.15 mm in all models) for the thicker specimen. Also here is the drop in load large. This larger load drop is probably attributed to the relatively lower displacement to failure for the scaled specimen, as the finer discretization otherwise would be expected to give a more gradual response.

In all cases, the failure is initiated underneath the load cylinders; first on the side with the displaced support and soon thereafter also below the second load cylinder. Damage can also be found in the centre of all specimens, but only for the scaled specimen there is a clear compressive failure that develops. Furthermore, the maximum compressive stress at the initial failure point is very similar in all models and corresponds to kinking initiation with a shear stress of ~10 MPa. This local shear stress, introduced by the transverse load, explains that the failure is initiated underneath the supports and not in the centre of the specimen.

In Fig. 26 the compressive strain is plotted for the base and scaled models at a prescribed roller displacement of ~7 mm. The relatively lower element and kink length in the scaled specimen leads to higher compaction of the elements and to higher compressive strains. At the max strain level of -0.27 in the base model the kink band is broadening whereas the -0.4 strain in the scaled model corresponds to the start of stiffening. Even a strain of -0.4 is far from the kinking initiation stress
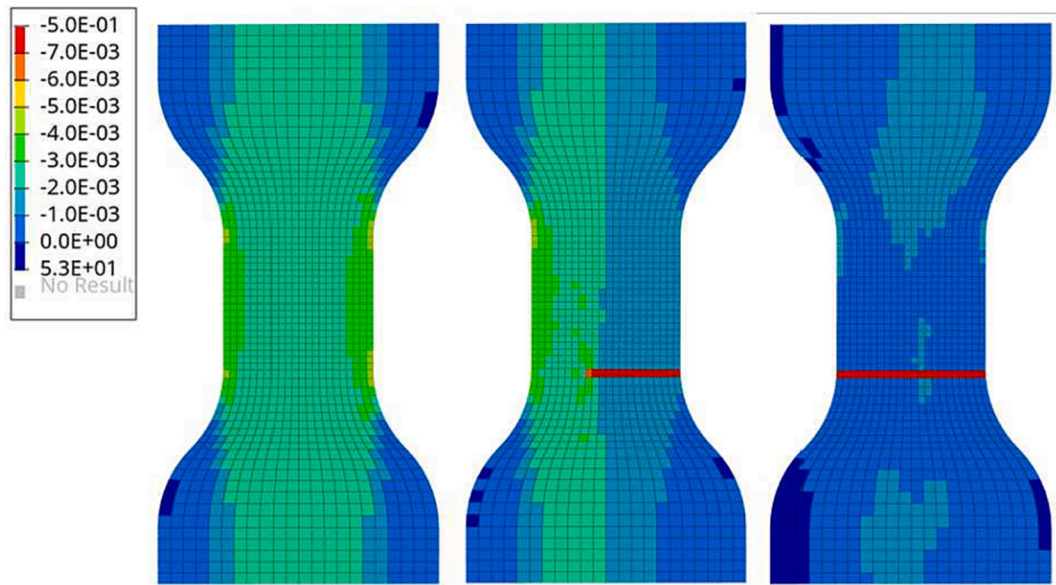
Fig. 21. Growth of kink band across the thickness in the 0.6 mm model during the load drop at the first load peak in Fig. 20.
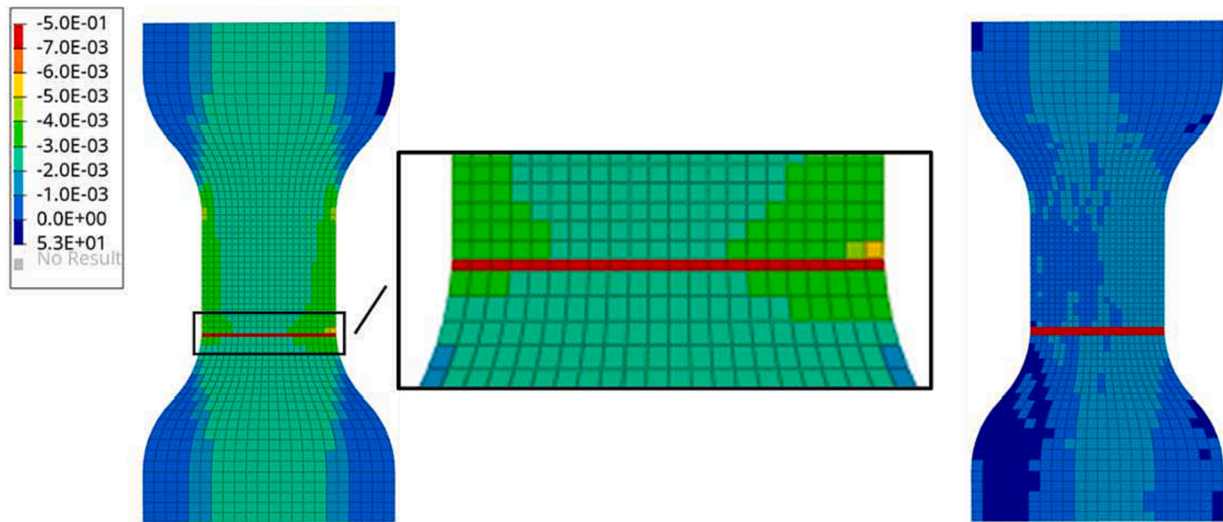

Fig. 22. Compressed first kink band in the 0.6 mm model just before and creation of a second band at the second load peak in Fig. 20.

(see Fig. 18) which is explained by that the stress discontinuity over the kinking element is large so that the compressive stress is well below the initial failure stress when the neighbouring elements start to kink.

In Fig. 27, the failure ratios, i.e. the ratio between maximum stress to uniaxial strength values, are shown for the axial tensile and through thickness shear stress components. The tensile strength is taken as 1,781 MPa and the through thickness shear strength 56 MPa, both values from Ref. [29]. The results in Fig. 27, including data both for the base model and the scaled model, are to be used below for a discussion of failure modes and comparison to literature. As can be seen, both the tensile and shear stress make a jump when kinking develops, with the shear stresses increasing more than the tensile stresses. There is basically no difference in the tensile response between the models, whereas the shear increases more for the base model than for the scaled model. In Fig. 28, the stress distribution at a failure ratio close to 1 is plotted for both axial tensile and through thickness shear.

As no experimental data exists the results from the analyses are here evaluated against general findings from literature. The maximum values in the load–displacement graph in Fig. 25 are ~10–15 % above the

failure initiation loads which, considering the distance of the integration point to the surface, means that the predicted maximum load is ~20–25 % higher than the failure load predicted by analytical means or by FE models assessing failure initiation at the upper surface. This is well in line with the results in Refs. [36–39]. Considering the results in Fig. 27, a failure mode of combined compression and shear is to be expected as the failure ratio in shear is higher than in tension. However, considering that e.g. the material used in Ref. [39] has a specified interlaminar shear strength of 100 MPa, or almost 80 % higher than the shear strength from Ref. [29], a tensile failure would most likely be predicted for that material. Hence, the proposed modelling of compression failure, incorporating a stress plateau and stiffening at large strains, will predict final failure by either tension or compression/shear depending on the ratio fibre tensile/shear strength of the composite material. These are the same failure modes that are seen in experiments [36,38,39] but further work is needed to asses if the proposed modelling can predict the correct failure mode for different materials. Though, the results presented here give no indication that there is an increased tendency for combined shear and compressive failure with increasing thickness as seen in
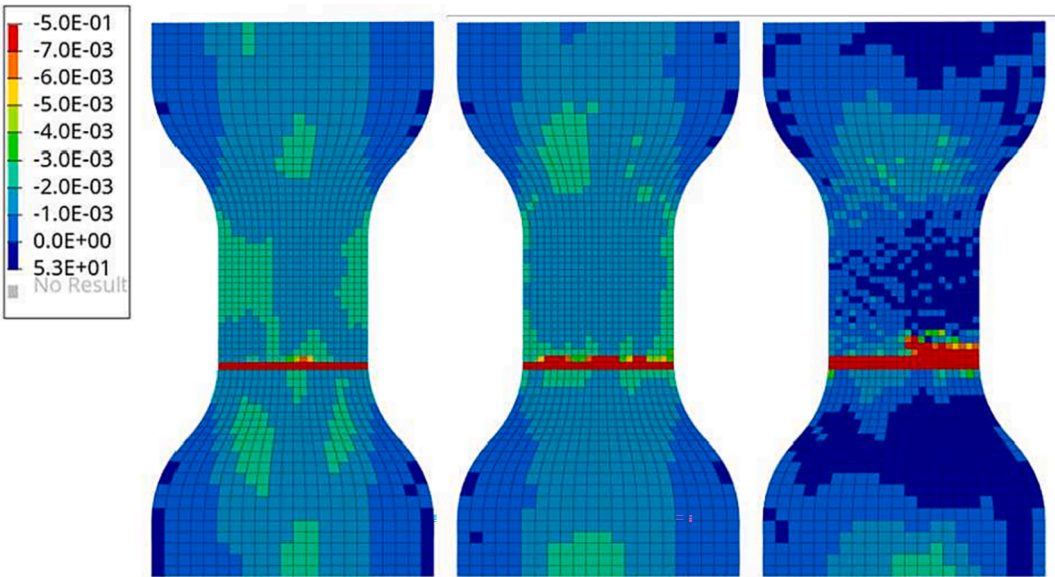
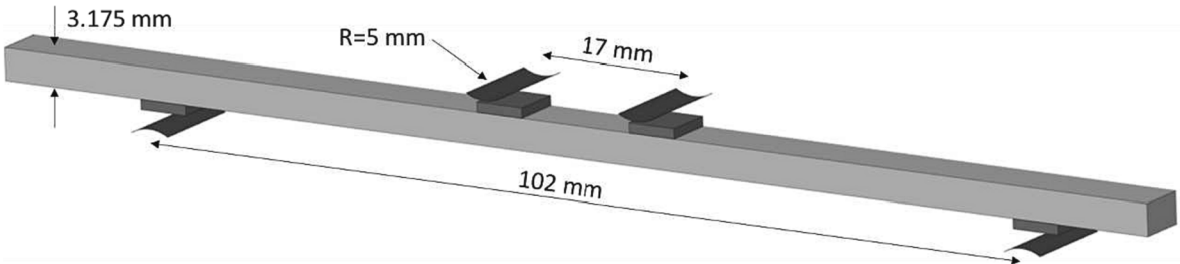**Fig. 23.** Unstable growth of kink band failure in the 0.6 mm model close to the final peak in Fig. 20.

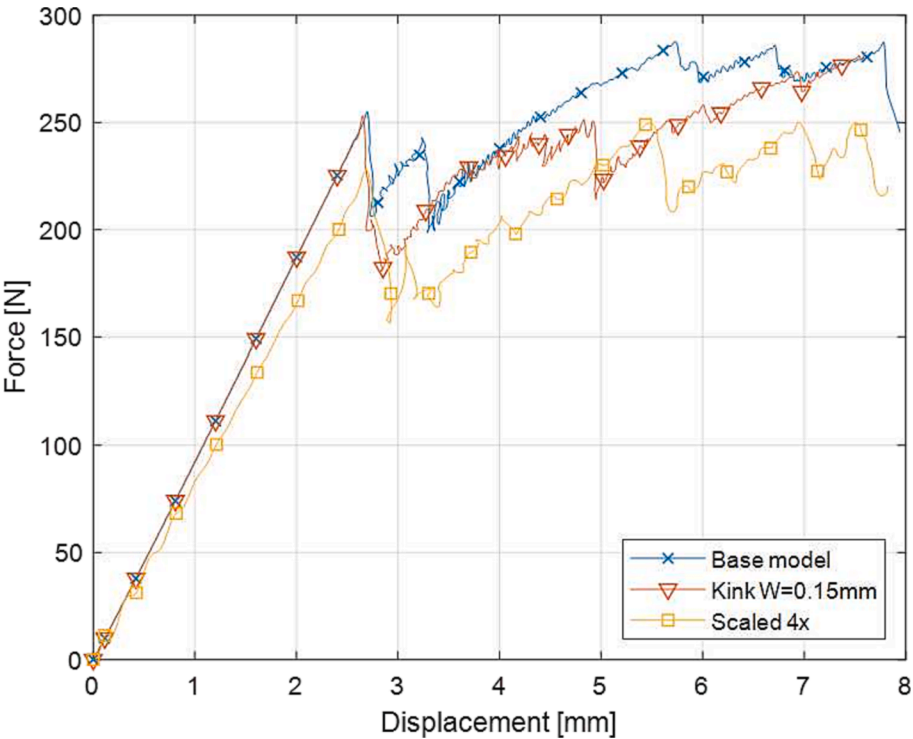
Fig. 24. Flexure simulation test set-up and geometry.

Fig. 25. Force displacement plots for the base model, the base model with lower kink band width and the 4 times scaled model.
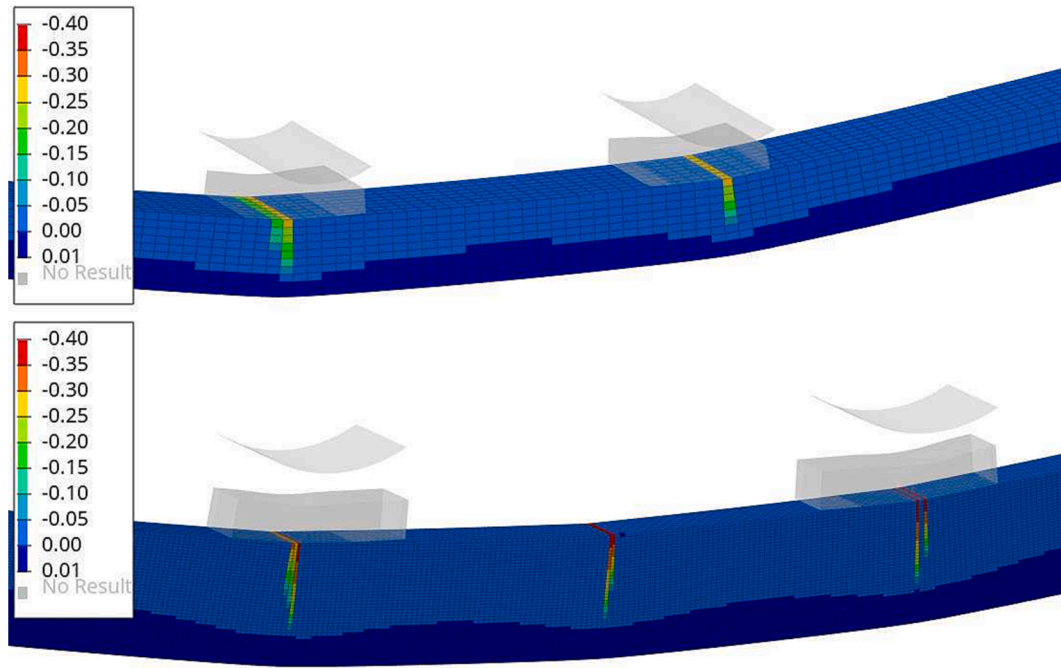
Fig. 26. Compressive strain plot for the base model (top) and the scaled model at a displacement of ~7 mm showing high strain values localized to areas with kinking failure.
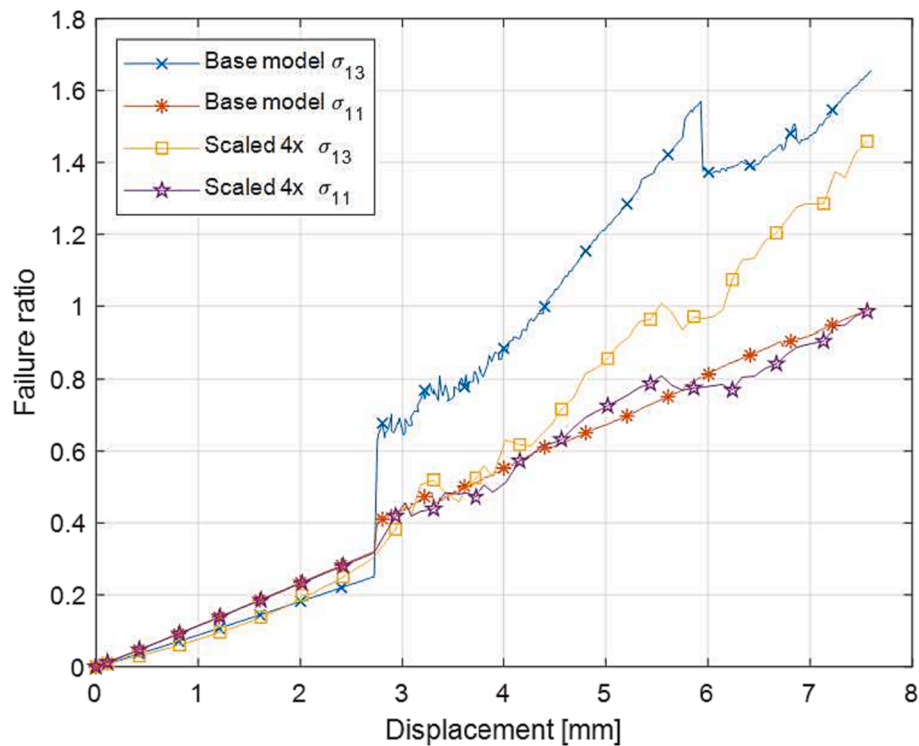

Fig. 27. Failure ratio of maximum axial tensile stress and maximum through thickness shear stress as function of beam displacement.

experiments [38,39]. It remains to be investigated if implementation of a mechanism for final failure in compression would influence this finding.

7. Conclusions and outlook

The application of continuum damage models that employ element erosion in composite crash and impact analyses effectively results in a loss of material volume and an introduction of voids in the material during damage evolution. This is a consequence of that in such models the stress is quickly reduced to a lower constant plateau value (or even zero), whereafter the element is deleted due to low stiffness or excessive deformations. In this work, an engineering model to describe kink band formation and growth is proposed, which includes a stiffening at larger strains thereby prohibiting excessive compressive deformation. In that way, there is no need for elements to be deleted. Instead, the increasing
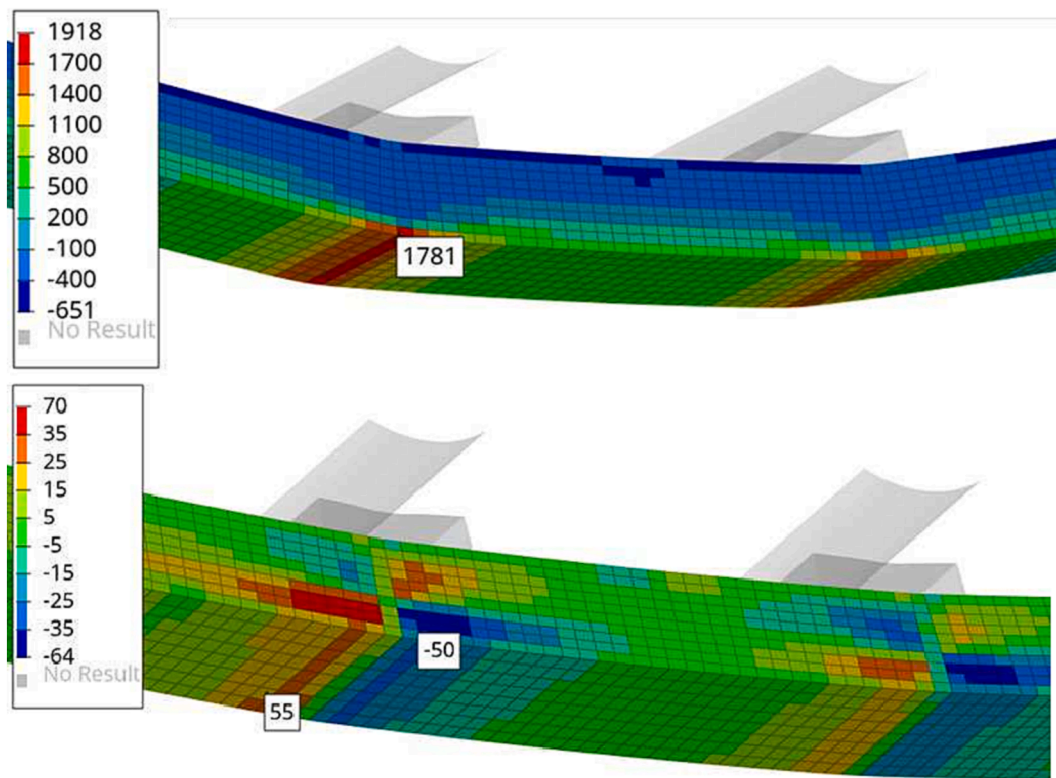
Fig. 28. Plots of axial stress (top) and through thickness shear stress (bottom) at the time of predicted failure.

load at high strains (mimicking compaction of damaged material) naturally allows the spreading of kink bands to adjacent elements.

The base of the current kinking formulation is similar to other widely applied kinking theories, but the kinematics are different due to assumptions made regarding how the influence of kink band angle β and its effect on the kink band volume is included in the model. The assumption on the effect of kink band angle on the kinking behaviour is also carried forward to facilitate a 3D FE-implementation with a strain decomposition based on kink band width. Together with an addition of a model for kink band broadening, the proposed total model also allows the kink band to grow through the element before the element stiffens due to the large compressive strains. Complemented with a failure initiation criterion that includes the effect of global shear stress, the model and its implementation display the following characteristics and advantages:

- The model is physically-based and requires only standard material properties as input and requires no intralaminar fracture toughness test data for calibration.
- After initial softening the kinking stress starts to increase progressively with increased compressive strain. As demonstrated in a uniaxial case, at ~60 % compression, the compressive stress is again high enough to initiate kinking failure in adjacent elements.
- The fibre rotation in the kink band at the point when the compressive stiffness starts to increase again is ~35°. At the initiation of kind band broadening, this angle is ~50°. Interestingly enough, typical values of lock-up angles reported in the literature are most often within this interval.
- In both the kinking formulation and the FE implementation, the sliding of the top and bottom of the kink band – due to the fibre rotation in the kink band – is neglected. This allows a pure compressive deformation of the elements during kinking under large deformations, without any spurious element shear deformations.

- The model for kink band broadening, together with the implementation of growth of kink band width using a strain decomposition in the element, results in an element size dependent length of the plateau with constant stress. This in turn significantly decreases the mesh dependence of results when modelling crushing.
- Regularisation of the kinking response based on the initial kink band width makes the formulation mesh objective.
- A large deformation formulation based on Green–Lagrange strains is used for the implementation. With some modifications it is shown to give a response in accordance with the underlying kinking model.
- For compressive failure under high shear loads, the kinking model is predicting higher values at 10 % compressive strain than what is predicted at failure initiation by the Budiansky and LARC05 compressive failure criteria.

The objective with the compressive failure model presented here is not to model the kinking failure in detail, including the direct effect of fibre rotation in the kink band and the angle of the kink band on the local deformations. It is instead developed to model the compressive response beyond the failure initiation, for confined compaction or crushing using less details. Due to the stiffening at large compressive strains, the model prohibits element deletion e.g. due to excessive deformations that without element deletion would result in a significant reduction of critical time step size in the explicit FE simulations.

Presented numerical results shows the ability of the model to transfer progressive kinking between elements, but also the possible impact from including confined compression effects on the predicted response of composite structures loaded in bending. Moreover, although the model is physically inspired when considering the simplifications performed it is positive that it still predicts an increase in compressive stress close to the expected lock-up angle.

It should be emphasised that the failure initiation criterion needed modification, since the compressive stress required to drive the kinking process for larger values of applied shear stress was higher than the

failure stress predicted by the Budiansky failure initiation criterion. However, as the validation and improvement of models for predicting the dependence of applied shear stresses on the kinking initiation stress is out of scope of this study, it remains to be investigated how the kinking results under high shear stress match experimental data. If the kinking predictions would match, new or modified theories for compressive failure under large shear stresses, consistent with the current kinking formulation, would need to be further developed.

The ultimate objective of the work presented here is to develop a constitutive formulation suitable for modelling compressive failure for the case when the composite material is confined in the crushing region, thereby experiencing large compaction. This would constitute an important development for the finite element simulation of progressive damage and failure in composites and the results presented in this paper shows that the kinking model goes a long way to model this type of compressive failure. However, such a model also needs a mechanism for final failure. A mechanism that allows the material to shear off in the through-thickness direction when neighbouring plies are not able to provide sufficient support (e.g. due to delamination). Conceptually, this could be the full cross-section of the laminate shearing away or single laminas separated by delaminations to show more of a brooming mode of failure. The development of this type of failure mechanism is planned as the next part of the current work.

CRediT authorship contribution statement

Niklas Jansson: Conceptualization, Methodology, Software, Formal analysis, Investigation, Funding acquisition, Writing – original draft. **Martin Fagerström:** Writing – review & editing, Resources, Supervision, Funding acquisition.

Declaration of Competing Interest

The authors declare that they have no known competing financial interests or personal relationships that could have appeared to influence the work reported in this paper.

Data availability

Data will be made available on request.

Acknowledgements

References

[1] Bogenfeld R, Kreikemeier J, Wille T. Review and benchmark study on the analysis of low-velocity impact on composite laminates. Eng Fail Anal 2018;86:72–99. https://doi.org/10.1016/j.engfailanal.2017.12.019.

[2] Israr HA, Jye WK, Rivallant S. Numerical modelling strategies for composite structures crashworthiness: a review. J Adv Res Mater Sci 2018;42(1):8–23.

[3] Falzon BG. Computational modelling of the crushing of carbon fibre-reinforced polymer composites. Phil Trans R Soc A 2022;380(2232):20210336. https://doi.org/10.1098/rsta.2021.0336.

[4] Livermore Software Technology Corporation (LSTC). LS-DYNA user's manual version R12.0, volume II: material models; 2020.

[5] Pinho ST, Iannucci L, Robinson P. Physically-based failure models and criteria for laminated fibre-reinforced composites with emphasis on fibre kinking: Part I: development. Compos A: Appl Sci Manuf 2006;37(1):63–73. https://doi.org/10.1016/j.compositesa.2005.04.016.

[6] Soutis C. Compressive strength of composite laminates with an open hole: effect of ply blocking. J Compos Mater 2013;47(20–21):2503–12. https://doi.org/10.1177/0021998312466122.

[7] Catalanotti G, Xavier J, Camanho PP. Measurement of the compressive crack resistance curve of composites using the size effect law. Compos A: Appl Sci Manuf 2014;56:300–7. https://doi.org/10.1016/j.compositesa.2013.10.017.

[8] Pinho S, Darvizeh R, Robinson P, Schuecker C, Camanho P. Material and structural response of polymer-matrix fibre-reinforced composites. J Compos Mater 2012;46 (19–20):2313–41. https://doi.org/10.1177/0021998312454478.

[9] Gutkin R, Pinho ST, Robinson P, Curtis PT. Micro-mechanical modelling of shear-driven fibre compressive failure and of fibre kinking for failure envelope generation in CFRP laminates. Compos Sci Technol 2010;70(8):1214–22. https://doi.org/10.1016/j.compscitech.2010.03.009.

[10] Argon AS. Fracture of composites. In: Treatise on materials science & technology. Elsevier; 1972. p. 79–114. Accessed: Jun. 26, 2023. [Online]. Available: https://linkinghub.elsevier.com/retrieve/pii/B9780123418012500072.

[11] Budiansky B. Micromechanics. Comput Struct 1983;16(1–4):3–12. https://doi.org/10.1016/0045-7949(83)90141-4.

[12] Budiansky B, Fleck NA. Compressive failure of fibre composites. J Mech Phys Solids 1993;41(1):183–211. https://doi.org/10.1016/0022-5096(93)90068-Q.

[13] Skovsgaard SPH, Jensen HM. Steady-state kink band propagation in layered materials. J Appl Mech 2018;85(6):061005. https://doi.org/10.1115/1.4039573.

[14] Matsuo T, Kageyama K. Compressive failure mechanism and strength of unidirectional thermoplastic composites based on modified kink band model. Compos A: Appl Sci Manuf 2017;93:117–25. https://doi.org/10.1016/j.compositesa.2016.11.018.

[15] Sun W, Vassilopoulos AP, Keller T. Experimental investigation of kink initiation and kink band formation in unidirectional glass fiber-reinforced polymer specimens. Compos Struct 2015;130:9–17. https://doi.org/10.1016/j.compstruct.2015.04.028.

[16] Daniel IM, Hsiao HM. Is there a thickness effect on compressive strength of unnotched composite laminates? In: Bažant ZP, Rajapakse YDS, editors. Fracture scaling. Dordrecht: Springer Netherlands; 1999. p. 143–58. Accessed: Apr. 06, 2023. [Online]. Available: http://link.springer.com/10.1007/978-94-011-4659-3_8.

[17] Gutkin R, Pinho ST, Robinson P, Curtis P. Physical mechanisms associated with initiation and propagation of kink-bands. Proceedings of the 13th European conference on composite materials (ECCM13). 2008.

[18] Moran PM, Liu XH, Shih CF. Kink band formation and band broadening in fiber composites under compressive loading. Acta Metall Mater 1995;43(8):2943–58. https://doi.org/10.1016/0956-7151(95)00001-C.

[19] Moran PM, Shih CF. Kink band propagation and broadening in ductile matrix fiber composites: experiments and analysis. Int J Solids Struct 1998;35(15):1709–22. https://doi.org/10.1016/S0020-7683(97)00138-8.

[20] Vogler TJ, Kyriakides S. On the axial propagation of kink bands in fiber composites: Part i experiments. Int J Solids Struct 1999;36(4):557–74. https://doi.org/10.1016/S0020-7683(98)00029-8.

[21] Sivashanker S, Fleck NA, Sutcliffe MPF. Microbuckle propagation in a unidirectional carbon fibre-epoxy matrix composite. Acta Mater 1996;44(7):2581–90. https://doi.org/10.1016/1359-6454(95)00410-6.

[22] Budiansky B, Fleck NA, Amazigo JC. On kink-band propagation in fiber composites. J Mech Phys Solids 1998;46(9):1637–53. https://doi.org/10.1016/S0022-5096(97)00042-2.

[23] Costa S, Fagerström M, Olsson R. Development and validation of a finite deformation fibre kinking model for crushing of composites. Compos Sci Technol 2020;197:108236. https://doi.org/10.1016/j.compscitech.2020.108236.

[24] Vogler TJ, Kyriakides S. On the initiation and growth of kink bands in fiber composites: Part I. Experiments. Int J Solids Struct 2001;38(15):2639–51. https://doi.org/10.1016/S0020-7683(00)00174-8.

[25] Chaplin CR. Compressive fracture in unidirectional glass-reinforced plastics. Composites 1978;9(3):206. https://doi.org/10.1016/0010-4361(78)90374-9.

[26] Larsson R, Gutkin R, Rouhi MS. Damage growth and strain localization in compressive loaded fiber reinforced composites. Mech Mater 2018;127:77–90. https://doi.org/10.1016/j.mechmat.2018.09.001.

[27] Basu S, Waas A, Ambur D. Compressive failure of fiber composites under multi-axial loading. J Mech Phys Solids 2006;54(3):611–34. https://doi.org/10.1016/j.jmps.2005.09.004.

[28] Gutkin R, Costa S, Olsson R. A physically based model for kink-band growth and longitudinal crushing of composites under 3D stress states accounting for friction. Compos Sci Technol 2016;135:39–45. https://doi.org/10.1016/j.compscitech.2016.09.002.

[29] Bru T, Hellström P, Gutkin R, Ramantani D, Peterson G. Characterisation of the mechanical and fracture properties of a uni-weave carbon fibre/epoxy non-crimp fabric composite. Data Brief 2016;6:680–95. https://doi.org/10.1016/j.dib.2016.01.010.

[30] Edgren F, Asp LE, Joffe R. Failure of NCF composites subjected to combined compression and shear loading. Compos Sci Technol 2006;66(15):2865–77. https://doi.org/10.1016/j.compscitech.2006.02.021.

[31] Herráez M, Fernández A, Lopes CS, González C. Strength and toughness of structural fibres for composite material reinforcement. Phil Trans R Soc A 2016;374(2071):20150274. https://doi.org/10.1098/rsta.2015.0274.

[32] Svensson D, Alfredsson KS, Stigh U, Jansson NE. Measurement of cohesive law for kink-band formation in unidirectional composite. Eng Fract Mech 2016;151:1–10. https://doi.org/10.1016/j.engfracmech.2015.10.040.

[33] Wilhelmsson D, Mikkelsen LP, Fæster S, Asp LE. Influence of in-plane shear on kink-plane orientation in a unidirectional fibre composite. Compos A: Appl Sci Manuf 2019;119:283–90. https://doi.org/10.1016/j.compositesa.2019.01.018.

[34] Puck A, Kopp J, Knops M. Guidelines for the determination of the parameters in Puck's action plane strength criterion. Compos Sci Technol 2002;62(3):371–8. https://doi.org/10.1016/S0266-3538(01)00202-0.

[35] Wilhelmsson D, Mikkelsen LP, Fæster S, Asp LE. X-ray tomography data of compression tested unidirectional fibre composites with different off-axis angles. Data Brief 2019;25:104263. https://doi.org/10.1016/j.dib.2019.104263.

[36] Koc M, Sonmez FO, Ersoy N, Cinar K. Failure behavior of composite laminates under four-point bending. J Compos Mater 2016;50(26):3679–97. https://doi.org/10.1177/0021998315624251.

[37] Burgani TDS, Alaie S, Tehrani M. Modeling flexural failure in carbon-fiber-reinforced polymer composites. J Compos Sci 2022;6(2):33. https://doi.org/10.3390/jcs6020033.

[38] Wisnom MR. The effect of specimen size on the bending strength of unidirectional carbon fibre-epoxy. Compos Struct 1991;18(1):47–63. https://doi.org/10.1016/0263-8223(91)90013-O.

[39] Carbajal N, Mujika F. Determination of compressive strength of unidirectional composites by three-point bending tests. Polym Test 2009;28(2):150–6. https://doi.org/10.1016/j.polymertesting.2008.11.003.